Phase-field simulation of multiple fluid vesicles with a consistently energy-stable implicit–explicit method

Junxiang Yang[a], Junseok Kim[b,*]

[a] *School of Computer Science and Engineering, Faculty of Innovation Engineering, Macau University of Science and Technology, Macao Special Administrative Region of China*
[b] *Department of Mathematics, Korea University, Seoul, 02841, Republic of Korea*

Abstract

When certain polymer amphiphiles and phospholipids are dispersed in a liquid, these molecules combine to form various closed bilayer structures known as multiple vesicles. The specific structures of these vesicles play fundamental roles in cytobiology and drug transportation. To model the multiple lipid vesicles in a fluid environment, we use the multi-phase conservative Allen–Cahn-type equations with approximately area-preserving penalty terms to capture the vesicle interfaces and the incompressible Navier–Stokes equations to describe the evolution of velocity and pressure. To efficiently simulate this complex coupled fluid system, we introduce several time-dependent variables to transform the total energy functional and the governing equations into equivalent forms. Based on these equivalent models, we develop a totally decoupled, energy-stable, and temporally second-order accurate time-marching scheme. A consistency-enhanced technique is utilized to correct the computed energy so that a more accurate solution is obtained. The time-discretized energy stability can be analytically estimated and the solution algorithm in each time step is easy to implement. Various numerical experiments, such as multi-component vesicles with different initial shapes, multiple vesicles in shear flow, and multiple vesicles in complex domains, are performed to verify the accuracy, stability, and capability of our proposed method.
© 2023 Elsevier B.V. All rights reserved.

1. Introduction

In cytobiology science, the vesicle membrane plays an important role in the transmission of biological signals, the storage of enzymes, metabolism, and other functions. To achieve different biological functions, the composition of lipids, proteins, and cholesterol in the membrane varies significantly. Previous experimental and numerical research [1–4] has observed that the surrounding environment can significantly affect the morphology of the vesicle membrane. Moreover, the incompressibility of the membrane was considered to contribute to the conservation of surface area. The balance of osmotic pressure between the interior and exterior of the membrane leads to the

---

conservation of vesicle volume. Therefore, an appropriate mathematical model should take into account the constant surface area and volume.

By considering the vesicle membrane as the interface between two incompressible fluids, the phase-field (diffuse-interface) method provides an effective approach to capture the deformation and motion of the interface. In the phase-field method, the fluid interface can be represented by the zero level-set value of an order parameter. The order parameter takes the values of 1 and −1 with respect to the bulk fluids inside and outside the interface, respectively. By adopting an elastic bending energy functional, Du et al. [5] presented a phase-field-type binary fluid vesicle model. The dynamic evolution of the membrane was driven by the minimization of elastic bending energy. Later, many researchers developed surface area-preserving methods based on the penalty approach [6] and the Lagrange multiplier approach [7,8]. To reduce the stiffness caused by the penalty term, Shin et al. [9] proposed a hybrid penalty-Lagrange multiplier method for computing the binary phase-field vesicle model. Based on a similar binary model, Zou et al. [10] developed a linear, second-order time-accurate, and energy-stable scheme using the scalar auxiliary variable (SAV) method. Recently, Ashour et al. [11] presented a fluid flow-coupled phase-field model for the hydrodynamics of vesicle doublets.

In micro-vessel stenosis or micro-fluid devices, the deformation and adhesion of multiple vesicles should be investigated. The binary phase-field model may not be suitable because when two vesicles are close enough, they tend to merge and form a larger vesicle. However, in reality, the coalescence of real vesicles does not occur. To resolve this problem, the vector-valued phase-field approach [12–16] emerges as a suitable choice for developing a multiple vesicles model. Based on a vector-valued H^{-1}-gradient flow model, Lee [17] proposed a hybrid phase-field immersed boundary method (IBM) for simulating cell divisions. Chen and Yang [18] constructed a multi-phase fluid vesicle system and designed an associated linearly energy-stable method based on the SAV approach. In each time step, several linear equations need to be solved to achieve totally decoupled computations. Compared to the traditional linear semi-implicit method, their algorithm requires extra computational costs.

In most phase-field models, the minimization of energy functionals drives the evolutionary dynamics of solutions. To obtain physically consistent results, a natural requirement is to design energy dissipation-preserving (energy-stable) numerical methods. For some standard phase-field equations, such as the Cahn–Hilliard (CH) equation, the Allen–Cahn (AC) equation, and the phase-field crystal (PFC) equation, many energy-stable methods have been developed. For example, the convex splitting method [19–22], the stabilization method [23,24], and the auxiliary variable methods [25–28]. However, for the fluid flow-coupled multi-component vesicles system, developing energy-stable schemes by directly using the convex splitting method and the stabilization method is not trivial. Although the classical SAV-type auxiliary variable method [10,18] can easily construct unconditionally energy-stable schemes by introducing auxiliary variables and eliminating the effect of nonlinear terms, the consistency between the original energy and the modified energy is not guaranteed theoretically. To this end, we aim to develop an efficient, totally decoupled, and linear energy-stable scheme with temporally second-order accuracy for the incompressible fluid flow-coupled N-phase ($N \geq 2$) phase-field vesicle model. The vesicle membranes are represented by the zero level-sets of multiple order parameters. The penalty technique and the Lagrange multiplier are adopted to achieve the conservation of surface area and volume, respectively. By coupling with the incompressible Navier–Stokes equations, the effect of hydrodynamics on vesicles can be reflected.

To design the energy-stable time-marching scheme, several time-dependent variables are introduced to transform the original energy and the governing equations into equivalent forms. Based on the equivalent model, totally decoupled linear implicit–explicit scheme is proposed. To improve the consistency between the original energy and its modified (numerical) version, a simple correction technique is presented. In each time step, the corrected energy dissipation property can be easily estimated. It is worth noting that the computational efficiency of the proposed scheme is comparable to that of typical semi-implicit schemes which do not satisfy the energy dissipation law. We do not need additional computational costs to have the decoupling of different variables. By modifying the momentum equation with a simple immersed boundary-type penalty term, the proposed method is also practical to simulate multiple vesicles flowing through irregular domains.

The rest parts of this work are organized as follows. In Section 2, we introduce the mathematical model of the hydrodynamically coupled multiple vesicles system. The equivalent forms and consistently energy-stable linear scheme are presented in Section 3. In Section 4, extensive numerical simulations are performed to validate the performance of our method. The conclusions are drawn in Section 5.

2. Hydrodynamically coupled multiple vesicles model

In this section, we first introduce the derivation of multiple vesicles model based on the phase-field theory in Section 2.1. To describe the evolution of fluid flow, the incompressible Navier–Stokes (NS) equations are adopted in Section 2.2. By adding convection and surface tension into the phase-field equation and momentum equation, we obtain the coupled multiple fluid vesicles system (governing equations). In Section 2.3, the associated energy dissipation property of the coupled system is estimated. In the next section, the temporal discretization of the governing equations will be introduced in detail.

2.1. Derivation of multiple vesicles model

Based on the preliminary ideas of phase-field modeling for lipid vesicles [5,29,30], the zero level-sets of multiple phase-field functions (order parameters ϕ_i, $i = 1, 2, \ldots, N$) are used to represent the membranes of multiple vesicles. Inside the vesicle and in the exterior region (ambient liquid), we let $\phi_i = 1$ and -1, respectively. To achieve a smooth transition across the phase interface (membrane), the phase-field functions are defined as $\phi_i = \tanh(d_i/(\sqrt{2}\epsilon))$, where d_i is the signed distance function between the interface and any arbitrary spatial position. The thickness of the interfacial transition is affected by a small positive constant ϵ. For most phase-field equations, the governing equations are obtained from a total free energy functional. Each term in the energy functional plays a role of specific physical constraint and the minimization of energy decides the evolutionary dynamics of the solution. For the multiple vesicles with closed membrane structures, the minimization of the elastic bending energy reflects the decrease of the mean curvature of each membrane. In a two-dimensional or three-dimensional domain Ω, the elastic bending energy is defined as [31,32]

$$E_{elastic}(\boldsymbol{\phi}) = \sum_{i=1}^{N} \int_{\Gamma_i} \kappa H_i^2 \, ds, \tag{1}$$

where $\boldsymbol{\phi} = (\phi_1, \phi_2, \ldots, \phi_N)$, $\boldsymbol{x}$ is the spatial variable, Γ_i is the ith membrane surface, κ is the bending rigidity, and H is the mean curvature of the ith membrane surface. With the definition of local equilibrium state (i.e., $\phi_i = \tanh(d_i/(\sqrt{2}\epsilon))$), we have the equality $0.25(\phi_i^2 - 1)^2 = 0.5\epsilon^2|\nabla\phi_i|^2$. The mean curvature is defined as $H_i = \nabla \cdot (\nabla\phi_i/|\nabla\phi_i|)$, and it can be expanded to be

$$H_i = \nabla\left(\frac{1}{|\nabla\phi_i|}\right) \cdot \nabla\phi_i + \frac{\Delta\phi_i}{|\nabla\phi_i|} = \nabla\left(\frac{\sqrt{2}\epsilon}{1 - \phi_i^2}\right) \cdot \nabla\phi_i + \frac{\Delta\phi_i}{|\nabla\phi_i|}$$

$$= \frac{2\sqrt{2}\epsilon\phi_i|\nabla\phi_i|^2}{(1 - \phi_i^2)^2} + \frac{\Delta\phi_i}{|\nabla\phi_i|} = \frac{\sqrt{2}\phi_i}{\epsilon} + \frac{\sqrt{2}\epsilon\Delta\phi_i}{(1 - \phi_i^2)^2} = \frac{\sqrt{2}}{\epsilon(1 - \phi_i^2)}\left(\epsilon^2\Delta\phi_i - \phi_i^3 + \phi_i\right).$$

With a regularized Dirac delta function $\delta(\phi_i) = 3(\phi_i^2 - 1)^2/(4\sqrt{2}\epsilon)$ [33], the elastic bending energy can be recast to be

$$E_{elastic}(\boldsymbol{\phi}) = \sum_{i=1}^{N} \int_{\Omega} \kappa H_i^2 \delta(\phi_i) \, d\boldsymbol{x} = \frac{3\kappa}{2\sqrt{2}\epsilon^3} \sum_{i=1}^{N} \int_{\Omega} \left(\epsilon^2\Delta\phi_i - \phi_i^3 + \phi_i\right)^2 \, d\boldsymbol{x}$$

$$= \frac{3\kappa}{2\sqrt{2}\epsilon^5} \sum_{i=1}^{N} \int_{\Omega} (\Delta\phi_i - f(\phi_i))^2 \, d\boldsymbol{x}, \tag{2}$$

where $f(\phi_i) = F'(\phi_i) = (\phi_i^3 - \phi_i)/\epsilon^2$ and $F(\phi_i) = (\phi_i^2 - 1)^2/(4\epsilon^2)$. Let the bending rigidity be $\kappa = \sqrt{2}\epsilon^6/3$, the final version of the elastic bending energy is

$$E_{elastic}(\boldsymbol{\phi}) = \sum_{i=1}^{N} \int_{\Omega} \frac{\epsilon}{2} (\Delta\phi_i - f(\phi_i))^2 \, d\boldsymbol{x}. \tag{3}$$

The minimization of Eq. (3) corresponds to the decrease of the mean curvature of each membrane.

The conservation of surface area is a fundamental physical property of vesicle. Let the area function of the ith vesicle be [18]

$$A(\phi_i) = \epsilon \int_{\Omega} \left(\frac{1}{2}|\nabla\phi_i|^2 + F(\phi_i)\right) \, d\boldsymbol{x},$$
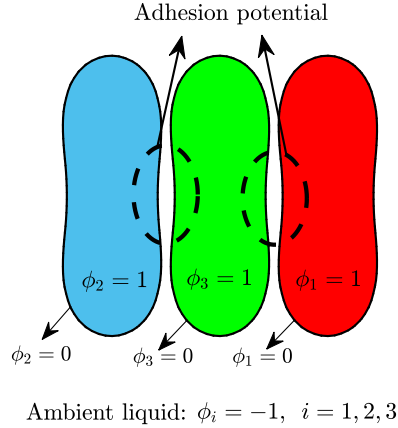
Fig. 1. Schematic illustration of multi-component fluid vesicles.

where the linear term $|\nabla \phi_i|^2$ contributes to the diffusion of the interface and the nonlinear term $F(\phi_i)$ accounts for the separation of liquids inside and outside the membrane. The competition between diffusion and separation leads to the formation of a limited diffuse thickness across the membrane interface. Let the initial surface area of the ith vesicle be $B_i = A(\phi_i|_{t=0})$. To preserve surface area, we introduce the following penalty energy:

$$E_{area}(\boldsymbol{\phi}) = \sum_{i=1}^{N} \frac{M}{2} \left(A(\phi_i) - B_i \right)^2 . \tag{4}$$

Here, $M > 0$ is a penalty constant. The magnitude of convergence between $A(\phi_i)$ and its initial area B_i is reflected by the value of M. The minimization of Eq. (4) indicates the conservation of surface area.

Due to the impenetrability of the membrane, penetration is not allowed when multiple vesicles are close to each other. To suppress overlap between vesicles, we introduce the following adhesion potential energy:

$$E_{adhesion}(\boldsymbol{\phi}) = - \int_{\Omega} \sum_{i,j=1, i<j}^{N} \frac{C_{ij}}{2\epsilon} (\phi_i^2 - 1)(\phi_j^2 - 1) \, d\boldsymbol{x}. \tag{5}$$

Here, $C_{ij} = C_{ji} > 0$ influences the magnitude of the adhesion force. The schematic illustration of multiple fluid vesicles is shown in Fig. 1. In the bulk phases of the vesicle and ambient liquid, the adhesion energy is absent because $\phi_i = 0$ or $\phi_j = 0$. When an overlap between bulk phases occurs, the adhesion energy is close to zero because $\phi_i \to 0$ or $\phi_j \to 0$. When vesicles adhere to each other, Eq. (5) takes its minimum value. Therefore, the minimization of this energy leads to vesicles adhesion.

By combining Eqs. (3)–(5) together, the total free energy functional of the multiple vesicles system reads as

$$E(\boldsymbol{\phi}) = \lambda \left(\underbrace{\sum_{i=1}^{N} \int_{\Omega} \frac{\epsilon}{2} \left(\Delta \phi_i - f(\phi_i) \right)^2 \, d\boldsymbol{x}}_{\text{I}} + \underbrace{\sum_{i=1}^{N} \frac{M}{2} (A(\phi_i) - B_i)^2}_{\text{II}} - \underbrace{\int_{\Omega} \sum_{i,j=1, i<j}^{N} \frac{C_{ij}}{2} (\phi_i^2 - 1)(\phi_j^2 - 1) \, d\boldsymbol{x}}_{\text{III}} \right), \tag{6}$$

where $\lambda > 0$ is a scaling parameter. Because $E(\boldsymbol{\phi})$ is a functional with respect to each ϕ_i, the governing equation of ϕ_i can be derived based on the energy variational principle. To do this, we first define the chemical potential of the ith vesicle as $\mu_i = \delta E(\boldsymbol{\phi})/\delta \phi_i$, where δ represents the variational derivative operator. Let $\mathcal{E}(\phi)$ be a functional with respect to function ϕ, ψ be an arbitrary smooth function and l be a small variation. The variational equality can be defined as

$$\lim_{l \to 0} \frac{\mathcal{E}(\phi + l\psi) - \mathcal{E}(\phi)}{l} = \int_{\Omega} \frac{\delta \mathcal{E}(\phi)}{\delta \phi} \psi \, d\boldsymbol{x}. \tag{7}$$

Let us consider three typical forms of energy functional: $\mathcal{E}_1(\phi) = \int_\Omega \frac{1}{2}|\nabla\phi|^2 \, d\boldsymbol{x}$, $\mathcal{E}_2(\phi) = \int_\Omega \frac{1}{2}|\Delta\phi|^2 \, d\boldsymbol{x}$, and $\mathcal{E}_3(\phi) = \int_\Omega N(\phi) \, d\boldsymbol{x}$, where $N(\phi)$ is a general nonlinear functional. It can be observed that the total free energy Eq. (6) is a combination of the aforementioned three functionals. For convenience, we only present the calculations of variational derivative of $\mathcal{E}_1(\phi)$, $\mathcal{E}_2(\phi)$, and $\mathcal{E}_3(\phi)$. The calculation of $\delta E(\boldsymbol{\phi})/\delta\phi_i$ is straightforward. By substituting $\mathcal{E}_1(\phi)$ into Eq. (7), we have

$$\lim_{l \to 0} \frac{1}{l} \int_\Omega \left[\frac{1}{2}|\nabla(\phi + l\psi)|^2 - \frac{1}{2}|\nabla\phi|^2 \right] d\boldsymbol{x}$$
$$= \lim_{l \to 0} \frac{1}{l} \int_\Omega \left[\frac{1}{2}\nabla(\phi + l\psi) \cdot \nabla(\phi + l\psi) - \frac{1}{2}\nabla\phi \cdot \nabla\phi \right] d\boldsymbol{x}$$
$$= \lim_{l \to 0} \frac{1}{l} \int_\Omega \left(l\nabla\phi \cdot \nabla\psi + \frac{l^2}{2}\nabla\psi \cdot \nabla\psi \right) d\boldsymbol{x}$$
$$= \int_\Omega \nabla\phi \cdot \nabla\psi \, d\boldsymbol{x} = \int_{\partial\Omega} (\mathbf{n} \cdot \nabla\phi)\psi \, ds - \int_\Omega (\Delta\phi)\psi \, d\boldsymbol{x} = \int_\Omega \frac{\delta\mathcal{E}_1(\phi)}{\delta\phi}\psi \, d\boldsymbol{x}.$$

By considering $\mathbf{n} \cdot \nabla\phi = 0$ on $\partial\Omega$, we get $-\int_\Omega (\Delta\phi)\psi \, d\boldsymbol{x} = \int_\Omega \frac{\delta\mathcal{E}_1(\phi)}{\delta\phi}\psi \, d\boldsymbol{x}$. Because ψ is an arbitrary function with the desired regularity, the variational derivative of $\mathcal{E}_1(\phi)$ to ϕ reads as

$$\frac{\delta\mathcal{E}_1(\phi)}{\delta\phi} = -\Delta\phi. \tag{8}$$

By substituting $\mathcal{E}_2(\phi)$ into Eq. (7), we have

$$\lim_{l \to 0} \frac{1}{l} \int_\Omega \left[\frac{1}{2}|\Delta(\phi + l\psi)|^2 - \frac{1}{2}|\Delta\phi|^2 \right] d\boldsymbol{x}$$
$$= \lim_{l \to 0} \frac{1}{l} \int_\Omega \left[\frac{1}{2}\Delta(\phi + l\psi) \cdot \Delta(\phi + l\psi) - \frac{1}{2}\Delta\phi \cdot \Delta\phi \right] d\boldsymbol{x}$$
$$= \lim_{l \to 0} \frac{1}{l} \int_\Omega \left(l\Delta\phi \cdot \Delta\psi + \frac{l^2}{2}\Delta\psi \cdot \Delta\psi \right) d\boldsymbol{x}$$
$$= \int_\Omega \Delta\phi \cdot \Delta\psi \, d\boldsymbol{x} = \int_\Omega (\Delta^2\phi)\psi \, d\boldsymbol{x} = \int_\Omega \frac{\delta\mathcal{E}_2(\phi)}{\delta\phi}\psi \, d\boldsymbol{x}.$$

Thus, the variational derivative of $\mathcal{E}_2(\phi)$ to ϕ can be written as

$$\frac{\delta\mathcal{E}_2(\phi)}{\delta\phi} = \Delta^2\phi. \tag{9}$$

By substituting $\mathcal{E}_3(\phi)$ into Eq. (7), we have

$$\lim_{l \to 0} \frac{1}{l} \int_\Omega [N(\phi + l\psi) - N(\phi)] \, d\boldsymbol{x} = \lim_{l \to 0} \frac{1}{l} \int_\Omega l\psi \left[\frac{N(\phi + l\psi) - N(\phi)}{l\psi} \right] d\boldsymbol{x}$$
$$= \int_\Omega N'(\phi)\psi \, d\boldsymbol{x} = \int_\Omega \frac{\delta E_3(\phi)}{\delta\phi}\psi \, d\boldsymbol{x},$$

where $N'(\phi)$ is the derivative of $N(\phi)$ to ϕ. The variational derivative of $\mathcal{E}_3(\phi)$ to ϕ can be written as

$$\frac{\delta\mathcal{E}_3(\phi)}{\delta\phi} = N'(\phi). \tag{10}$$

Based on the aforementioned calculations, we take the variational derivation of Eq. (6) to ϕ_i, the chemical potential of the ith vesicle can be defined as

$$\mu_i = \frac{\delta E(\boldsymbol{\phi})}{\delta\phi_i}$$
$$= \lambda \left[\epsilon(\Delta - f'(\phi_i))(\Delta\phi_i - f(\phi_i)) + \epsilon M(A(\phi_i) - B_i)(-\Delta\phi_i + f(\phi_i)) - \sum_{j=1, j\neq i}^{N} C_{ij}\phi_i(\phi_j^2 - 1) \right], \tag{11}$$

where $f'(\phi_i) = (3\phi_i^2 - 1)/\epsilon^2$. By utilizing the L^2-gradient flow approach [34–36] (i.e., $\frac{\partial\phi_i}{\partial t} = -\gamma\mu_i$) and the Lagrange multiplier-type mass compensation strategy, the governing equations of the multi-component vesicles

read as

$$\frac{\partial \phi_i}{\partial t} = -\gamma(\mu_i - \beta_i), \quad i = 1, 2, \ldots, N, \tag{12}$$

$$\mu_i = \lambda \left[\epsilon(\Delta - f'(\phi_i))(\Delta\phi_i - f(\phi_i)) + \epsilon M(A(\phi_i) - B_i)(-\Delta\phi_i + f(\phi_i)) - \sum_{j=1, j\neq i}^{N} C_{ij}\phi_i(\phi_j^2 - 1) \right], \tag{13}$$

where γ is a positive constant, $\beta_i = \frac{1}{|\Omega|}\int_\Omega \mu_i \, dx$ is a Lagrange multiplier related to the ith component, $|\Omega|$ represents the total area/volume of the domain. By multiplying 1 to Eq. (12) and taking the integral operation, it is easy to obtain the mass conservation property, i.e., $\frac{d}{dt}\int_\Omega \phi_i \, dx = 0$. We define the volume of a vesicle as $V(\phi_i) = \int_\Omega (\phi_i + 1)/2 \, dx$, it is evident that $V(\phi_i)$ is also conserved.

Remark 2.1. In this work, ϕ_i is an indicator function. In the interior of the ith vesicle, $\phi_i = 1$. Let $\phi_i = -1$ in the ambient liquid. Because the volume of a real vesicle cannot be negative, we define the inner volume $V(\phi_i) = \int_\Omega (\phi_i + 1)/2 \, dx$ just for representing the volume enclosed by the diffuse interface. In actual computation, we still adopt the global definition of total volume (i.e., $\int_\Omega \phi_i \, dx$) instead of $V(\phi_i)$. Therefore, the definition of $V(\phi_i)$ does not affect the numerical results.

2.2. Incompressible Navier–Stokes equations

To describe the evolution of fluid flow, we herein adopt the following incompressible NS equations

$$\frac{\partial \boldsymbol{u}}{\partial t} + \boldsymbol{u} \cdot \nabla \boldsymbol{u} = -\nabla p + \frac{1}{Re}\Delta \boldsymbol{u}, \tag{14}$$

$$\nabla \cdot \boldsymbol{u} = 0. \tag{15}$$

Here, $\boldsymbol{u}$ is the velocity field. In 2D or 3D space, the velocity components are (u, v) or (u, v, w), respectively. The pressure is p. The Reynolds number is Re. Eq. (15) is the divergence-free (incompressible) condition. The momentum equation is obtained based on the Newton's second law. For detailed description of numerical method of the NS equations, please refer to [37] and references therein. If we assume $\boldsymbol{u} = 0$ on the domain boundary $\partial\Omega$, we can derive that the evolution of incompressible NS equations dissipates the kinetic energy $\int_\Omega \frac{1}{2}|\boldsymbol{u}|^2 \, dx$. Because the estimation is similar to that in Eq. (22), we omit this to keep the article short.

2.3. Coupled system and its energy dissipation property

To reflect the dynamic deformation of multiple vesicles in fluid environment, Eqs. (12) and (13) are coupled with the incompressible NS equations. The coupled fluid vesicle system is written as

$$\frac{\partial \phi_i}{\partial t} + \nabla \cdot (\boldsymbol{u}\phi_i) = -\gamma(\mu_i - \beta_i), \quad i = 1, 2, \ldots, N, \tag{16}$$

$$\mu_i = \lambda \left[\epsilon(\Delta - f'(\phi_i))(\Delta\phi_i - f(\phi_i)) + \epsilon M(A(\phi_i) - B_i)(-\Delta\phi_i + f(\phi_i)) - \sum_{j=1, j\neq i}^{N} C_{ij}\phi_i(\phi_j^2 - 1) \right], \tag{17}$$

$$\frac{\partial \boldsymbol{u}}{\partial t} + \boldsymbol{u} \cdot \nabla \boldsymbol{u} = -\nabla p + \frac{1}{Re}\Delta \boldsymbol{u} + \sum_{i=1}^{N} \mu_i \nabla\phi_i, \tag{18}$$

$$\nabla \cdot \boldsymbol{u} = 0. \tag{19}$$

The second term in Eq. (16) represents the advection of fluid on vesicles. The last term in Eq. (18) plays a role of surface tensions. The derivation of a similar form of surface tension can refer to [38]. On all domain boundaries, we consider the periodic or the following conditions

$$\boldsymbol{u}|_{\partial\Omega} = 0, \quad \nabla\phi_i \cdot \mathbf{n}|_{\partial\Omega} = 0, \quad \nabla\Delta\phi_i \cdot \mathbf{n}|_{\partial\Omega} = 0, \quad i = 1, 2, \ldots, N,$$

where $\mathbf{n}$ is the unit outward normal vector to $\partial\Omega$. For two functions f_a and f_b, their L^2-inner product is defined as $(f_a, f_b) = \int_\Omega f_a f_b \, d\boldsymbol{x}$. The associated L^2-norm is $\|f_a\|^2 = (f_a, f_a)$. By following the similar estimations in [18], we can take the L^2-inner product of each term in Eq. (16) with μ_i for $i = 1, 2, \ldots, N$ and obtain

$$\sum_{i=1}^{N} \left(\frac{\partial \phi_i}{\partial t}, \mu_i \right) + \sum_{i=1}^{N} \int_\Omega \nabla \cdot (\mathbf{u}\phi_i)\mu_i \, d\boldsymbol{x} = -\gamma \sum_{i=1}^{N} \|\mu_i - \beta_i\|^2. \tag{20}$$

Here, we use $\int_\Omega \mu_i - \beta_i \, d\boldsymbol{x} = 0$. The detailed derivation can be found in [18]. By taking the L^2-inner product of each term in Eq. (17) with $\partial \phi_i / \partial t$ for $i = 1, 2, \ldots, N$, we have

$$\sum_{i=1}^{N} \left(\mu_i, \frac{\partial \phi_i}{\partial t} \right) = \frac{d}{dt} E(\boldsymbol{\phi}). \tag{21}$$

By taking the L^2-inner product of each term in Eq. (18) with $\boldsymbol{u}$, we get

$$\frac{d}{dt} \int_\Omega \frac{1}{2} |\boldsymbol{u}|^2 \, d\boldsymbol{x} - \sum_{i=1}^{N} \int_\Omega \mu_i \nabla \phi_i \cdot \boldsymbol{u} \, d\boldsymbol{x} = -\frac{1}{Re} \|\nabla \boldsymbol{u}\|^2, \tag{22}$$

where the integration by parts, divergence-free condition (i.e., Eq. (19)), $\int_\Omega \boldsymbol{u} \cdot \nabla \boldsymbol{u} \cdot \boldsymbol{u} \, d\boldsymbol{x} = 0$, and $\int_\Omega \nabla p \cdot \boldsymbol{u} \, d\boldsymbol{x} = 0$ are used. These two equalities are estimated as follows

$$\int_\Omega \boldsymbol{u} \cdot \nabla \boldsymbol{u} \cdot \boldsymbol{u} \, d\boldsymbol{x} = \int_\Omega (u \ v \ w) \cdot \boldsymbol{u} \cdot \nabla \boldsymbol{u} \, d\boldsymbol{x}$$

$$= \int_\Omega uu\frac{\partial u}{\partial x} + uv\frac{\partial u}{\partial y} + uw\frac{\partial u}{\partial z} + vu\frac{\partial v}{\partial x} + vv\frac{\partial v}{\partial y} + vw\frac{\partial v}{\partial z} + wu\frac{\partial w}{\partial x} + wv\frac{\partial w}{\partial y} + ww\frac{\partial w}{\partial z} \, d\boldsymbol{x}$$

$$= \int_\Omega \left(uu\frac{\partial u}{\partial x} + vu\frac{\partial v}{\partial x} + wu\frac{\partial w}{\partial x} \right) + \left(uv\frac{\partial u}{\partial y} + vv\frac{\partial v}{\partial y} + wv\frac{\partial w}{\partial y} \right) + \left(uw\frac{\partial u}{\partial z} + vw\frac{\partial v}{\partial z} + ww\frac{\partial w}{\partial z} \right) \, d\boldsymbol{x}$$

$$= \int_\Omega \frac{u}{2} \frac{\partial \|\boldsymbol{u}\|^2}{\partial x} + \frac{v}{2} \frac{\partial \|\boldsymbol{u}\|^2}{\partial y} + \frac{w}{2} \frac{\partial \|\boldsymbol{u}\|^2}{\partial z} \, d\boldsymbol{x} = \int_\Omega \boldsymbol{u} \cdot \nabla \frac{\|\boldsymbol{u}\|^2}{2} \, d\boldsymbol{x}$$

$$= \int_{\partial\Omega} \frac{\|\boldsymbol{u}\|^2}{2} \cdot \boldsymbol{u} \cdot \mathbf{n} \, ds - \int_\Omega \frac{\|\boldsymbol{u}\|^2}{2} \nabla \cdot \boldsymbol{u} \, d\boldsymbol{x} = 0,$$

where the velocity boundary condition and the divergence-free condition (i.e., Eq. (19)) are used. By using the same conditions, we have

$$\int_\Omega \nabla p \cdot \boldsymbol{u} \, d\boldsymbol{x} = \int_{\partial\Omega} p \cdot \boldsymbol{u} \cdot \mathbf{n} \, ds - \int_\Omega p \nabla \cdot \boldsymbol{u} \, d\boldsymbol{x} = 0.$$

By combining Eqs. (20)–(22) together and using the equality $\int_\Omega \nabla \cdot (\mathbf{u}\phi_i)\mu_i - \mu_i \nabla \phi_i \cdot \boldsymbol{u} \, d\boldsymbol{x} = 0$, we derive the following energy dissipation property

$$\frac{d}{dt} E_O = \frac{d}{dt} E(\boldsymbol{\phi}) + \frac{d}{dt} \int_\Omega \frac{1}{2} |\boldsymbol{u}|^2 \, d\boldsymbol{x} = -\gamma \sum_{i=1}^{N} \|\mu_i - \beta_i\|^2 - \frac{1}{Re} \|\nabla \boldsymbol{u}\|^2 \le 0, \tag{23}$$

where E_O is the total energy, which consists of the free energy of phase-field functions and the kinetic energy. Without any external input of work, the aforementioned inequality indicates that the fluid flow-coupled multi-component vesicle system dissipates its total energy over time. Based on this basic physical property, the equivalent model and its consistent algorithm will be introduced in the next section.

3. Numerical solution algorithm

In this work, we aim to perform efficient and consistently energy dissipation-preserving (energy-stable) computations for the fluid vesicles system. To achieve this goal, the time-dependent variables: P, q, and Q are introduced to transform the original model (i.e., Eqs. (16)–(19)) into an equivalent form. Based on the equivalent equations, the energy dissipation property of associated time-marching scheme will be straightforwardly proved. Let $P = P(t) = E_O + D$, where D is a positive constant to make the value of P be positive. Moreover, we define

$q = P/(E_O + D)$ and $Q = q(2 - q)$ such that the exact values of q and Q are 1. With the definitions of P, the energy dissipation relationship (i.e., the equality in (23)) can be recast into the following equivalent form

$$\frac{dP}{dt} = -\frac{P}{E_O + D} \left(\gamma \sum_{i=1}^{N} \|\mu_i - \beta_i\|^2 + \frac{1}{Re} \|\nabla \boldsymbol{u}\|^2 \right). \tag{24}$$

The aforementioned equality holds because $P = E_O + D$, $E_O + D \neq 0$, and D is independent of time. Because P is an introduced extra variable, Eq. (24) provides an evolutionary equation for P to make the system be well-posed. By multiplying $Q \equiv 1$ to some specific terms in the original model, considering the definitions of q and Q, and taking Eq. (24) into account, the equivalent equations of the multi-phase fluid vesicles as follows:

$$\frac{\partial \phi_i}{\partial t} + Q\nabla \cdot (\boldsymbol{u}\phi_i) = -\gamma(\mu_i - \beta_i), \quad i = 1, 2, \ldots, N, \tag{25}$$

$$\mu_i = Q\lambda \left[\epsilon(\Delta - f'(\phi_i))(\Delta\phi_i - f(\phi_i)) + \epsilon M(A(\phi_i) - B_i)(-\Delta\phi_i + f(\phi_i)) - \sum_{j=1, j\neq i}^{N} C_{ij}\phi_i(\phi_j^2 - 1) \right], \tag{26}$$

$$\frac{\partial \boldsymbol{u}}{\partial t} + Q\boldsymbol{u} \cdot \nabla \boldsymbol{u} = -\nabla p + \frac{1}{Re}\Delta\boldsymbol{u} + Q \sum_{i=1}^{N} \mu_i \nabla\phi_i, \tag{27}$$

$$\nabla \cdot \boldsymbol{u} = 0, \tag{28}$$

$$Q = q(2 - q), \quad q = P/(E_O + D), \tag{29}$$

$$\frac{dP}{dt} = -\frac{P}{E_O + D} \left(\gamma \sum_{i=1}^{N} \|\mu_i - \beta_i\|^2 + \frac{1}{Re} \|\nabla \boldsymbol{u}\|^2 \right). \tag{30}$$

The same boundary conditions described in the previous section are used. For the new system, the energy dissipation property with respect to an equivalent energy P can be clearly observed from Eq. (30) because its right hand side is less than or equal to zero. Similar observations can be found in the work of [39].

3.1. Second-order time-accurate linear scheme

Let T be the total computation time and N^T be the number of time iterations. The uniform time step is defined as $\Delta t = T/N^T$. Let $(\cdot)^n$ be the approximation of a specific variable at $t = n\Delta t$. In each time step, the time-marching scheme consists of two stages. In the first stage, the second-order backward difference formula (BDF2) is adopted to temporally discretize Eqs. (25)–(30) as

Stage 1.

$$\frac{3\phi_i^{n+1} - 4\phi_i^n + \phi_i^{n-1}}{2\Delta t} + Q^{n+1}\nabla \cdot (\boldsymbol{u}^*\phi_i^*) = -\gamma \left(\mu_i^{n+1} - \beta_i^{n+1} \right), \quad i = 1, 2, \ldots, N, \tag{31}$$

$$\mu_i^{n+1} = Q^{n+1}\lambda[\epsilon(\Delta - f'(\phi_i^*))(\Delta\phi_i^* - f(\phi_i^*)) + \epsilon M(A(\phi_i^*) - B_i)(-\Delta\phi_i^* + f(\phi_i^*))$$
$$- \sum_{j=1, j\neq i}^{N} C_{ij}\phi_i^* ((\phi_j^*)^2 - 1)] + \frac{\lambda S_a}{\epsilon^3} \left(\phi_i^{n+1} - \phi_i^* \right) - \frac{\lambda S_b}{\epsilon} \Delta \left(\phi_i^{n+1} - \phi_i^* \right) + \epsilon\lambda S_c \Delta^2 \left(\phi_i^{n+1} - \phi_i^* \right), \tag{32}$$

$$\frac{3\tilde{\boldsymbol{u}}^{n+1} - 4\boldsymbol{u}^n + \boldsymbol{u}^{n-1}}{2\Delta t} + Q^{n+1}\boldsymbol{u}^* \cdot \nabla\boldsymbol{u}^* = -\nabla p^n + \frac{1}{Re}\Delta\boldsymbol{u}^* + Q^{n+1} \sum_{i=1}^{N} \mu_i^* \nabla\phi_i^*, \tag{33}$$

$$\frac{3\boldsymbol{u}^{n+1} - 3\tilde{\boldsymbol{u}}^{n+1}}{2\Delta t} = -\nabla \left(p^{n+1} - p^n \right), \tag{34}$$

$$\nabla \cdot \boldsymbol{u}^{n+1} = 0, \tag{35}$$

$$Q^{n+1} = q^{n+1} \left(2 - q^{n+1} \right), \quad q^{n+1} = \hat{P}^{n+1}/(E_O^* + D), \tag{36}$$

$$\frac{\hat{P}^{n+1} - P^n}{\Delta t} = -\frac{\hat{P}^{n+1}}{E_O^* + D} \left(\gamma \sum_{i=1}^{N} \|\mu_i^* - \beta_i^*\|^2 + \frac{1}{Re} \|\nabla \boldsymbol{u}^*\|^2 \right). \tag{37}$$

Here, $(\cdot)^* = 2(\cdot)^n - (\cdot)^{n-1}$. On $\partial\Omega$, we consider the periodic or the following boundary conditions

$$\boldsymbol{u}^{n+1}\cdot\mathbf{n}|_{\partial\Omega} = 0, \ \ \tilde{\boldsymbol{u}}^{n+1}|_{\partial\Omega} = 0, \ \ \nabla p^{n+1}\cdot\mathbf{n}|_{\partial\Omega} = 0, \ \ \nabla\phi_i^{n+1}\cdot\mathbf{n}|_{\partial\Omega} = 0, \ \ \nabla\Delta\phi_i^{n+1}\cdot\mathbf{n}|_{\partial\Omega} = 0, \ \ i = 1, 2, \ldots, N,$$

In Eq. (32), the last three terms are added to improve numerical stability, S_a, S_b, and S_c are positive stabilization parameters [18,38]. In Eq. (33), $\tilde{\boldsymbol{u}}^{n+1}$ is an intermediate velocity field which does not satisfy the divergence-free condition. In Eqs. (33) and (34), the second-order projection-type splitting strategy was used to decouple the computations of velocity and pressure. We note that Eq. (36) is a temporally first-order accurate scheme, the resulting q^{n+1} is a first-order approximation to 1, i.e.,

$$q^{n+1} = q(t^{n+1}) + C\Delta t = 1 + C\Delta t,$$

where C is a constant independent of the time step. From the definition of Q, we have

$$Q^{n+1} = q^{n+1}(2 - q^{n+1}) = (1 + C\Delta t)(1 - C\Delta t) = 1 - C^2\Delta t^2,$$

where Q^{n+1} is a second-order approximation to 1. In this sense, Eqs. (31)–(35) still maintain the second-order accuracy. We define a modified energy as $E_M^{n+1} = \hat{P}^{n+1} - D$. It is worth noting that $\hat{P}^{n+1}$ computed from Eq. (37) might deviate from its definition (i.e., $P = E_O + D$) when a relatively large time step is used. Thus, the computed Q^{n+1} will gradually deviate from it exact value 1. This inconsistency between the numerical scheme and the original model definitely leads to inaccurate results. To fix this problem, we need to improve the consistency between $\hat{P}^{n+1}$ and $E_O^{n+1} + D$. After the computations in stage 1, the following stage should be performed to make the necessary correction.

Stage 2.

$$P^{n+1} = \xi_o \hat{P}^{n+1} + (1 - \xi_o)\left(E_O^{n+1} + D\right), \ \ \xi_o \in \mathcal{H}, \tag{38}$$

where

$$\mathcal{H} = \left\{ \xi \in [0, 1] \ \middle| \ \frac{P^{n+1} - \hat{P}^{n+1}}{\Delta t} \le -\vartheta^{n+1}\left(\gamma\sum_{i=1}^{N}\|\mu_i^{n+1} - \beta_i^{n+1}\|^2 + \frac{1}{Re}\|\nabla\boldsymbol{u}^{n+1}\|^2\right) \right. \tag{39}$$

$$\left. + \frac{\hat{P}^{n+1}}{E_O^* + D}\left(\gamma\sum_{i=1}^{N}\|\mu_i^* - \beta_i^*\|^2 + \frac{1}{Re}\|\nabla\boldsymbol{u}^*\|^2\right) \right\}. \tag{40}$$

Let $P^{n+1} - D$ be the corrected energy. By combining Eq. (37) and the aforementioned inequality, we get

$$\frac{P^{n+1} - P^n}{\Delta t} \le -\vartheta^{n+1}\left(\gamma\sum_{i=1}^{N}\|\mu_i^{n+1} - \beta_i^{n+1}\|^2 + \frac{1}{Re}\|\nabla\boldsymbol{u}^{n+1}\|^2\right). \tag{41}$$

To obtain the corrected energy dissipation law, i.e., $P^{n+1} \le P^n$, it is clear that ϑ^{n+1} should be non-negative. For the set $\mathcal{H}$, we can easily check that it is not empty because $\xi = 1 \in \mathcal{H}$. By rewriting Eq. (38) with the inequality in (40), we have

$$\xi_o\left(\hat{P}^{n+1} - \left(E_O^{n+1} + D\right)\right) \le \hat{P}^{n+1} - \left(E_O^{n+1} + D\right) - \Delta t\vartheta^{n+1}\left(\gamma\sum_{i=1}^{N}\|\mu_i^{n+1} - \beta_i^{n+1}\|^2 + \frac{1}{Re}\|\nabla\boldsymbol{u}^{n+1}\|^2\right)$$

$$+ \frac{\Delta t\,\hat{P}^{n+1}}{E_O^* + D}\left(\gamma\sum_{i=1}^{N}\|\mu_i^* - \beta_i^*\|^2 + \frac{1}{Re}\|\nabla\boldsymbol{u}^*\|^2\right). \tag{42}$$

Based on the aforementioned inequality, four possible choices of ξ_0 and ϑ^{n+1} are listed as follows:
(a) If $\hat{P}^{n+1} = E_O^{n+1} + D$, ξ_o is set to be zero and

$$\vartheta^{n+1} = \frac{\hat{P}^{n+1}\left(\gamma\sum_{i=1}^{N}\|\mu_i^* - \beta_i^*\|^2 + \frac{1}{Re}\|\nabla\boldsymbol{u}^*\|^2\right)}{\left(E_O^* + D\right)\left(\gamma\sum_{i=1}^{N}\|\mu_i^{n+1} - \beta_i^{n+1}\|^2 + \frac{1}{Re}\|\nabla\boldsymbol{u}^{n+1}\|^2\right)};$$

(b) If $\hat{P}^{n+1} > E_O^{n+1} + D$, ξ_o is set to be zero and

$$
\vartheta^{n+1} = \frac{\hat{P}^{n+1} - \left(E_O^{n+1} + D\right)}{\Delta t \left(\gamma \sum_{i=1}^{N} \|\mu_i^{n+1} - \beta_i^{n+1}\|^2 + \frac{1}{Re}\|\nabla \mathbf{u}^{n+1}\|^2\right)}
$$
$$
+ \frac{\hat{P}^{n+1} \left(\gamma \sum_{i=1}^{N} \|\mu_i^* - \beta_i^*\|^2 + \frac{1}{Re}\|\nabla \boldsymbol{u}^*\|^2\right)}{\left(E_O^* + D\right) \left(\gamma \sum_{i=1}^{N} \|\mu_i^{n+1} - \beta_i^{n+1}\|^2 + \frac{1}{Re}\|\nabla \boldsymbol{u}^{n+1}\|^2\right)};
$$

(c) If $\hat{P}^{n+1} < E_O^{n+1} + D$ and

$$
\hat{P}^{n+1} - \left(E_O^{n+1} + D\right) + \frac{\Delta t \hat{P}^{n+1}}{E_O^* + D} \left(\gamma \sum_{i=1}^{N} \|\mu_i^* - \beta_i^*\|^2 + \frac{1}{Re}\|\nabla \boldsymbol{u}^*\|^2\right) \geq 0,
$$

ξ_o is set to be zero and ϑ^{n+1} takes the aforementioned value in (b).
(d) If $\hat{P}^{n+1} < E_O^{n+1} + D$ and

$$
\hat{P}^{n+1} - \left(E_O^{n+1} + D\right) + \frac{\Delta t \hat{P}^{n+1}}{E_O^* + D} \left(\gamma \sum_{i=1}^{N} \|\mu_i^* - \beta_i^*\|^2 + \frac{1}{Re}\|\nabla \boldsymbol{u}^*\|^2\right) < 0,
$$

ϑ^{n+1} is set to be zero and

$$
\xi_o = 1 - \frac{\Delta t \hat{P}^{n+1} \left(\gamma \sum_{i=1}^{N} \|\mu_i^* - \beta_i^*\|^2 + \frac{1}{Re}\|\nabla \boldsymbol{u}^*\|^2\right)}{\left(E_O^* + D\right) \left(E_O^{n+1} + D - \hat{P}^{n+1}\right)}.
$$

In most choices, $\xi_o = 0$ means P^{n+1} strictly equals to $E_O^{n+1} + D$. In the last case, P^{n+1} is an appropriate approximation to $E^{n+1} + D$ because ξ_o still locates at [0, 1]. After the correction in stage 2, the consistency is improved. Several numerical simulations in Section 4 will show the significance of this correction technique.

Remark 3.1. In this remark, we interpret the physical meanings of the four cases: (a)–(d) in stage 2. First, the possible choices of ξ_o and ϑ^{n+1} should satisfy the inequality (42). Moreover, we notice that $\hat{P}^{n+1}$, $E_O^{n+1} + D$, and $\frac{\Delta t \hat{P}^{n+1}}{E_O^* + D} \left(\gamma \sum_{i=1}^{N} \|\mu_i^* - \beta_i^*\|^2 + \frac{1}{Re}\|\nabla \boldsymbol{u}^*\|^2\right)$ on the right-hand side of inequality (42) are independent of ξ_o and ϑ^{n+1}. Therefore, the relationships between these three quantities are natural criteria for choosing possible values of ξ_o and θ^{n+1}. In case (a), $\hat{P}^{n+1} = E_O^{n+1} + D$ indicates that the modified energy calculated from stage 1, the corrected energy, and the original energy are strictly consistent. Thus, correction is not required and we can directly set $\xi_o = 0$. The specific choice of ϑ^{n+1} in case (a) eliminates the last two terms in inequality (42). The original inequality relationship still holds because it degenerates into $\hat{P}^{n+1} = E_O^{n+1} + D$. In case (b), when the modified energy is large than the original energy (i.e., $\hat{P}^{n+1} > E_O^{n+1} + D$), the specific choice of ϑ^{n+1} in case (b) eliminates all the right-hand side terms in inequality (42). To satisfy this inequality relationship, we should set $\xi_o = 0$ to eliminate the left-hand side. Thus, the corrected energy strictly equals to the original energy. In case (c), the modified energy is less than the original energy (i.e, $\hat{P}^{n+1} < E_O^{n+1} + D$), which makes the left-hand side of (42) be non-positive. Here, the approximate energy dissipate rate is $\gamma \sum_{i=1}^{N} \|\mu_i^* - \beta_i^*\|^2 + \frac{1}{Re}\|\nabla \boldsymbol{u}^*\|^2$. Case (c) indicates that the difference between the modified energy and the original energy plus the energy dissipate rate multiplying Δt is non-negative. However, the third term on the right-hand side of inequality (42) is non-positive. It is generally not trivial to judge if the signs of the right-hand side and the left-hand side are the same. To satisfy inequality (42), the simplest approach is to set a specific ϑ^{n+1} in case (c) to eliminate all terms on the right-hand side, and set ξ_o to enforce consistency between the corrected energy and the modified energy. In case (d), the right-hand side of inequality (42) is strictly negative and the left-hand side is non-positive. For this case, simply setting ξ_o cannot satisfy the inequality relationship. For convenience, we directly set $\vartheta^{n+1} = 0$ to eliminate the third term on the right-hand side. The specific choice of ξ_o in this case not only satisfies $\xi_o \in (0, 1)$ but also satisfies the inequality relationship because (42) becomes an equality in the form of $0 = 0$.

3.2. Time-discretized energy property

In this subsection, we estimate the corrected energy dissipation law by proving the following theorem.

Theorem. The solutions computed by stage 1 and stage 2 unconditionally dissipate the corrected energy in time, i.e., $P^{n+1} \leq P^n$ for any Δt.

Proof. By recasting Eq. (37), we get

$$\hat{P}^{n+1} = P^n \left/ \left[1 + \frac{\Delta t}{E_O^* + D} \left(\gamma \sum_{i=1}^{N} \|\mu_i^* - \beta_i^*\|^2 + \frac{1}{Re} \|\nabla \boldsymbol{u}^*\|^2 \right) \right] \right. . \tag{43}$$

From the aforementioned expression, we have $\hat{P}^1 \geq 0$ with the initial setting $P^0 \geq 0$. With $\xi_o \in [0, 1]$ and $E_O^1 + D \geq 0$, we derive $P^1 \geq 0$ from Eq. (38). By induction, $P^n \geq 0$ and $\hat{P}^{n+1} \geq 0$ can be obtained. Thus, Eq. (37) indicates that

$$\frac{\hat{P}^{n+1} - P^n}{\Delta t} = -\frac{\hat{P}^{n+1}}{E_O^* + D} \left(\gamma \sum_{i=1}^{N} \|\mu_i^* - \beta_i^*\|^2 + \frac{1}{Re} \|\nabla \boldsymbol{u}^*\|^2 \right) \leq 0.$$

This inequality denotes that $\hat{P}^{n+1}$ is consistently less than or equal to P^n. From Eq. (38), we have $P^{n+1} \geq 0$ because $\hat{P}^{n+1}$ and $E_O^* + D$ are non-negative. This conclusion indicates the lower boundedness of the corrected energy $P^{n+1} - D$. Based on preliminary discussions, the inequality (41) indicates that $P^{n+1} \leq P^n$. Because D is a constant independent of time, the dissipation law of corrected energy has been proved. $\square$

3.3. Implementation in each time step

In this subsection, we discuss the numerical implementation of our proposed scheme in one time step. In stage 1, we observe that ϕ_i^{n+1}, p^{n+1}, $\tilde{\boldsymbol{u}}^{n+1}$, and $\boldsymbol{u}^{n+1}$ are totally decoupled in time because Q^{n+1} can be first calculated from Eq. (36). To perform the calculations described in Eq. (36), $\hat{P}^{n+1}$ is calculated using Eq. (37) (i.e., Eq. (43)).

To update ϕ_i^{n+1}, we can substitute μ_i^{n+1} and $\beta_i^{n+1} = \frac{1}{|\Omega|} \int_\Omega \mu_i^{n+1} \, d\boldsymbol{x}$ in Eq. (31) with the expression of μ_i^{n+1} in Eq. (32). By utilizing the mass conservation property, the integration by parts, and the aforementioned boundary conditions for ϕ_i^{n+1} and $\Delta\phi_i^{n+1}$, we can eliminate the non-local terms: $\frac{1}{|\Omega|} \int_\Omega \frac{S_a \lambda}{\epsilon^3} (\phi_i^{n+1} - \phi_i^*) \, d\boldsymbol{x}$, $\frac{1}{|\Omega|} \int_\Omega \frac{S_b \lambda}{\epsilon} \Delta(\phi_i^{n+1} - \phi_i^*) \, d\boldsymbol{x}$, and $\frac{1}{|\Omega|} \int_\Omega \epsilon S_c \lambda \Delta^2(\phi_i^{n+1} - \phi_i^*) \, d\boldsymbol{x}$ in actual computations.

With the computed $\tilde{\boldsymbol{u}}^{n+1}$, we can obtain the following pressure Poisson equation by taking the divergence operation to Eq. (34)

$$\Delta p^{n+1} = \Delta p^n + \frac{3}{2\Delta t} \nabla \cdot \tilde{\boldsymbol{u}}^{n+1}, \tag{44}$$

where the time-discretized divergence-free condition (i.e., Eq. (35)) is used. By solving this Poisson equation with a linear multigrid method [37], the updated p^{n+1} can be obtained.

Finally, we can directly obtain P^{n+1} through a correction step in stage 2. To facilitate the interested readers, we summarize the numerical implementation in Algorithm 1.

In each time step, Algorithm 1 completes the step-by-step computations. The implementation is efficient because the calculations are linear and decoupled. Because the BDF2-type scheme requires the information at previous two time steps, the first-order backward Euler-type scheme [38] was adopted to perform the computations at $t = \Delta t$.

4. Numerical experiments

The previous section only focused on the description of the time-marching algorithm because the energy law in the fully discrete form can be similarly obtained as long as the discrete integration by parts is appropriately defined. In this section, various numerical simulations are performed to verify the accuracy, consistent stability, and capability of our method. The finite difference method [40–42] is adopted to discretize the equations in space. Unless otherwise specified, the 2D domain is $\Omega = (0, 2\pi) \times (0, 2\pi)$. Let $Re = 1$, $C_{ij} = 2\text{e}4$, $\epsilon = 0.05$, $\gamma = 0.05$,

---

Algorithm 1: Pseudocode of numerical implementation in each time step

---

Data: Input the computed information at n-th and $(n-1)$-th time steps

1   Explicitly compute $\hat{P}^{n+1}$ and Q^{n+1} from Eqs.(37) and (36), respectively;

2   Update ϕ_i^{n+1} and μ_i^{n+1} by solving Eqs. (31) and (32) with a multigrid algorithm;

3   **while** *residual > tolerance* **do**

4     $(\phi_{i,k}^{n+1,m+1}, \mu_{i,k}^{n+1,m+1})$ = Multigrid-cycle(k, $\phi_{i,k}^{n+1,m}$, $\mu_{i,k}^{n+1,m}$, s_a^n, s_b^n, v);

5   ⋆ Here, m and $m+1$ indicate the solutions before and after one multigrid cycle, k is the multigrid level, s_a^n and s_b^n are the source terms in Eqs. (31) and (32), v is the number of relaxation;

6   **end**

7   Update $\tilde{\boldsymbol{u}}^{n+1}$ from Eq. (33) with an iteration algorithm;

8   **while** *residual > tolerance* **do**

9     $\left(\frac{3}{2\Delta t} - \frac{1}{Re}\Delta\right)\tilde{\boldsymbol{u}}^{n+1} = \frac{4\boldsymbol{u}^n - \boldsymbol{u}^{n-1}}{2\Delta t} - Q^{n+1}\boldsymbol{u}^* \cdot \nabla\boldsymbol{u}^* - \nabla p^n + Q^{n+1}\sum_{i=1}^{N}\mu_i^*\nabla\phi_i^*$;

10   **end**

11   Update p^{n+1} from Eq. (44) with a multigrid algorithm;

12   **while** *residual > tolerance* **do**

13     $p_k^{n+1,m+1}$ = Multigrid-cycle(k, $p_k^{n+1,m}$, s_p^n, v);

14   ⋆ Here, m and $m+1$ indicate the solutions before and after once multigrid cycle, k is the multigrid level, $s_p^n = \Delta p^n + \frac{3}{2\Delta t}\nabla \cdot \tilde{\boldsymbol{u}}^{n+1}$ is the source term, v is the number of relaxation;

15   **end**

16   Update the divergence-free velocity $\boldsymbol{u}^{n+1}$ from Eq. (34) in an explicit manner;

17   Correct the energy from $P^{n+1} = \xi_o\hat{P}^{n+1} + (1-\xi_o)(E_O^{n+1} + D)$;

Result: Output the updated information at $(n+1)$-th time step

---

Table 1

L^2-errors and convergence rates for the solutions of ϕ_i $(i = 1, 2)$ and velocities.

Δt	$32\delta t$	$16\delta t$	$8\delta t$	$4\delta t$	$2\delta t$
ϕ_1:	8.61e−7	2.22e−7	5.73e−8	1.41e−8	2.89e−9
Rate		1.96	1.95	2.02	2.29	
ϕ_2:	8.51e−7	2.21e−7	5.74e−8	1.42e−8	2.90e−9
Rate		1.94	1.94	2.02	2.29	
u:	6.69e−6	1.56e−6	3.28e−7	7.29e−8	1.42e−8
Rate		2.10	2.24	2.17	2.36	
v:	6.73e−6	1.58e−6	3.30e−7	7.33e−8	1.42e−8
Rate		2.09	2.26	2.17	2.36	

$M = $ 1e4, $\lambda = $ 2e−3, and $D = 100$ for the simulations. In Sections 4.1–4.7, all variables along x-direction are periodic. On the top and bottom boundaries, zero-Neumann and no-slip boundary conditions are used for scalar variables and velocities, respectively.

4.1. Temporal accuracy test

In the first test, we verify the accuracy in time by refining the time step. In a 2D space, the initial conditions of two adjacent hydrodynamically coupled vesicles are defined in Appendix. We set the mesh size as 128×128, $S_a = S_b = 4$, and $S_c = 1$. To conduct quantitative comparison of accuracy, numerical reference solutions are obtained by using a finer time step of $\delta t = 0.01h^2$, where $h = \pi/64$ is the spatial step. The coarsest time step is set to be $32\delta t$. By refining the time step by a factor of two, a set of numerical solutions with different time steps at $t = 128\delta t$ are obtained. The L^2-norm of errors between the numerical and reference solutions is listed in Table 1. The results indicate that the proposed scheme indeed achieves temporally second-order accuracy for the solutions of ϕ_i $(i = 1, 2)$ and velocities.
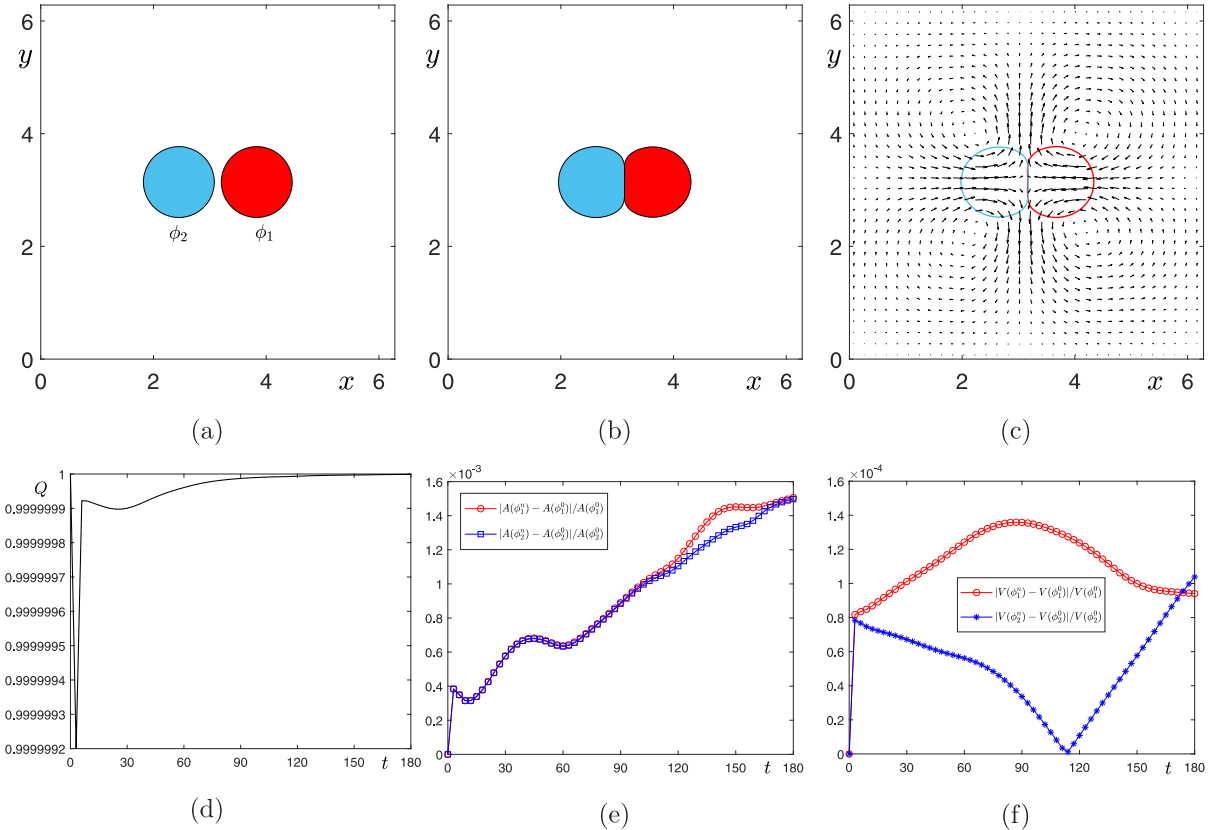
Fig. 2. Two adjacent fluid flow-coupled vesicles. The initial state, final state ($t = 180$), and velocity field are shown in (a), (b), and (c). The evolutions of Q, area ratio, and volume ratio are plotted in (d)–(f).

4.2. Energy dissipation law and consistency

Using the identical initial conditions and parameters as in the previous subsection, we herein investigate the evolutionary dynamics of energy curves under different time steps: $\Delta t = 0.01, 0.005, 0.0025$, and 0.00125. Fig. 2(a) displays the initial state of two adjacent vesicles, with a zero initial velocity field. In this test, circular initial shapes are considered. Note that the circular initial state has been used to simulate the tumor cell flowing through a tube [43] and the elastic membrane in contact with solid [44]. In Fig. 2(b), the snapshot of two vesicles at $t = 180$ is shown. Here, the interfaces are represented by the zero level-set of ϕ_i, that is, $\phi_i = 0$ ($i = 1, 2$). Due to the effect of adhesion potential, we observe that two vesicles adhere to each other. Fig. 2(c) plots the interfacial profiles and the velocity field at $t = 180$ with respect to $\Delta t = 0.01$. The equal contribution of surface tension leads to the symmetric distribution of velocities. In Fig. 2(d)–(f), the evolutions of Q, area ratio $|A(\phi_i^n) - A(\phi_i^0)|/A(\phi_i^0)$, and volume ratio $|V(\phi_i^n) - V(\phi_i^0)|/V(\phi_i^0)$ ($i = 1, 2$) are plotted, respectively. The results indicate that both area and volume are approximately conserved.

For the auxiliary variable Q, its exact value is 1. Therefore, we can multiply Q to some terms in equivalent system (i.e., Eqs. (25)–(28)) without changing the original dynamics. In actual computation, we cannot expect the numerical value of Q is strictly equal to 1 because the numerical computations only leads to approximate results. An appropriate numerical approximation of Q requires its numerical value should be close to 1. On the contrary, if the numerical value of Q deviates away from 1, the numerical method cannot accurately solve the original problem because the consistency between the original model and the equivalent model has been destroyed. In Fig. 2(d), the y-range represents the numerical value of Q. As we can observe, the numerical result is close to the exact solution (i.e., $Q = 1$). This also indicates that the proposed method achieves good consistency between the original model and the equivalent model.
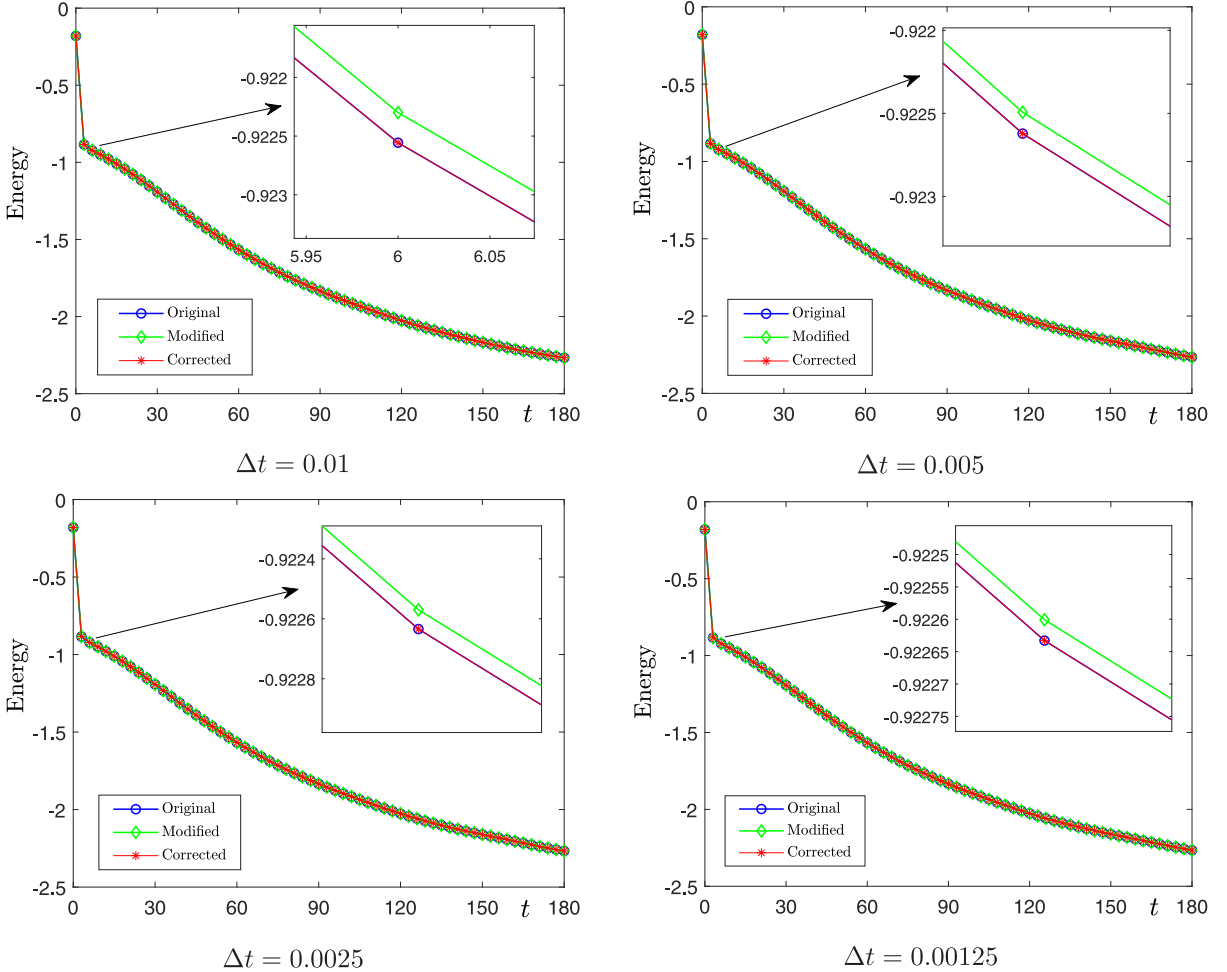
Fig. 3. Energy curves of original energy, modified energy, and corrected energy with respect to different time steps.

In the early stages of Fig. 2(d), a minor decrease in the numerical value of Q can be observed. For this phenomenon, we give the following two possible explanations: (i) The initial settings of velocity and pressure are artificial, which might not fit the real physical environment; (ii) The first-order accurate Euler scheme is used to perform the computation in the first time step. From the second time step, the BDF2 scheme works. Therefore, the difference between two temporal discretizations might cause a slight effect in the early stages. Although there is a slight fluctuation at early stage, the numerical value of Q and its exact result 1 are still highly consistent.

Fig. 3 shows the energy curves of the original energy, modified energy, and corrected energy with respect to different time steps. In each figure, the inset displays a local close-up view. Comparing with the difference between the original energy and the modified energy, it can be observed that the corrected energy and the original energy are highly consistent. This test indicates that the adopted correction technique indeed improves the consistency. In each case, the energy curves are dissipative over time.

To emphasize the necessity of the correction technique, we consider the same simulation with a relatively large time step of $\Delta t = 0.01$. The computations are performed until $t = 180$. Fig. 4(a) shows the interfacial profiles computed by both the method with and without correction technique. It is clear that the two vesicles do not adhere closely to each other if the correction technique is absent. To illustrate this, we also plot the evolution of Q in Fig. 2(b). For the simulation with the absence of correction, we observe that Q deviates significantly from its exact value 1. This indicates that the consistency between the original model and the equivalent model has been destroyed and the resulting simulation is not accurate. The blue line with open circles in Fig. 4(b) corresponds to the result in
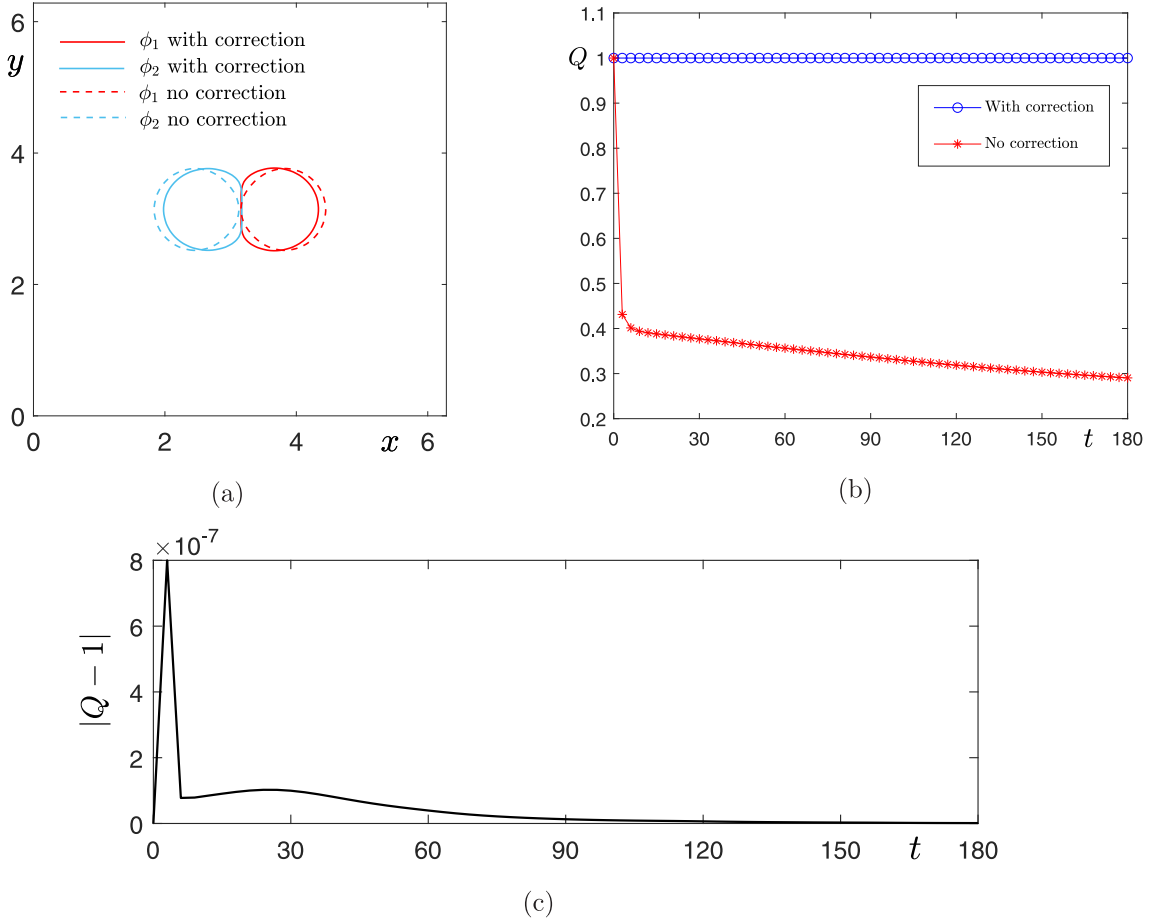
Fig. 4. Effect of correction technique. The interfacial profiles at $t = 180$ are shown in (a). The evolutions of Q are plotted in (b). The absolute error between Q and 1 is shown in (c). (For interpretation of the references to color in this figure legend, the reader is referred to the web version of this article.)

Fig. 2(d). When we plot the results with and without correction together, the slight drop of Q in Fig. 2(d) is hard to be observed. We also plot the absolute error $|Q - 1|$ in Fig. 4(c). As we can see, the correction algorithm makes the absolute error between Q and 1 be less than 1e−6. To obtain accurate results with a relatively large time step, the correction technique is necessary.

During early stages of evolution, we observe a sharp change in the energy curve and a slight drop in the value of Q. In our present simulations, the uniform time step $\Delta t = 0.01$ is used. To investigate the effect of the time step on the evolution of Q, we adopt the following adaptive time-stepping strategy based on energy changes [45]

$$\Delta t^{n+1} = \max\{\Delta_{\min}, \ \Delta t_{\max}/(1 + \nu E_O')\}, \tag{45}$$

where $\Delta t_{\min}$ and $\Delta t_{\max}$ are the minimum and maximum time steps, $E_O' = (E_O^n - E_O^{n-1})/\Delta t^n$ is the discrete time derivative of the total energy, $\nu = 0.01$ is a constant. Here, we set $\Delta t_{\max} = 0.01$ and $\Delta t_{\min} = 0.001$. The same simulation as shown in Fig. 2 is performed. The evolutions of Q with respect to uniform and adaptive time steps are plotted in Fig. 5. We observe that the difference is not obvious. The results indicate that the uniform time step $\Delta t = 0.01$ is an appropriate choice in this test. The resulting difference can be ignored because Q is highly close to its exact value 1.
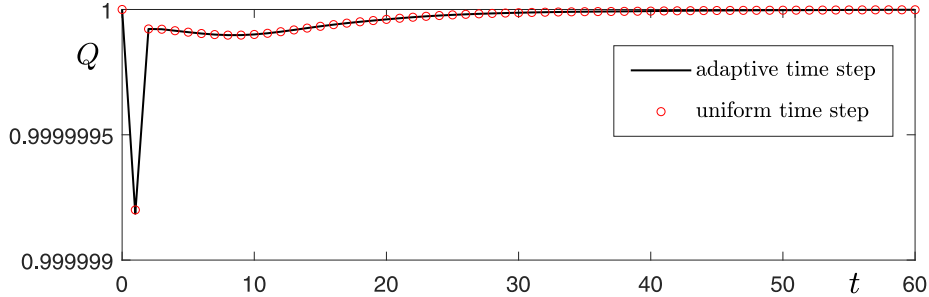
Fig. 5. Time evolutions of Q with respect to uniform time step and adaptive time step.
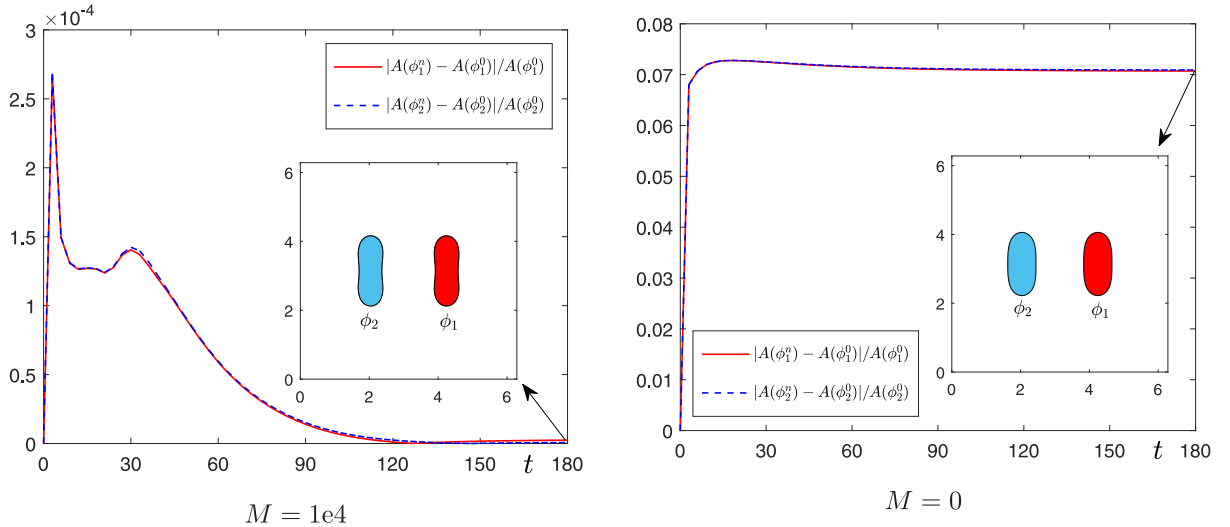

Fig. 6. Effect of penalty potential. In each figure, the inset shows the snapshot of ϕ_i $(i = 1, 2)$ at $t = 180$.

4.3. Effect of penalty potential

Area conservation is a basic property of lipid vesicles. The phase-field model introduces a penalty term to approximately satisfy the conservation of area. To test the effect of the penalty potential, we simulate the behavior of two separated vesicles within a fluid environment. The initial conditions are defined in Appendix. In this test, the rugby-like initial shapes are considered. This initial condition has been extensively adopted in previous researches [7,8,11,29,30] to evolve a final red blood cell-like membrane. The mesh size 128×128 is used. The time step is $\Delta t = 0.01$. Fig. 6 shows the evolution of the area ratio: $|A(\phi_i^n) - A(\phi_i^0)|/A(\phi_i^0)$ $(i = 1, 2)$ with respect to $M = 1e4$ and $M = 0$. Here, $M = 0$ indicates that the penalty potential is absent. In each figure, the inset shows the snapshot of the two vesicles at $t = 180$. From the results, we observe that $M = 0$ leads to non-conservative areas and ϕ_i does not evolve into a lipid vesicle-like shape. For $M = 0$, the relative error of surface area reaches an order of 0.07. On the contrary, the area conservation is approximately satisfied if $M = 1e4$ is used because the order of relative error is less than $3e-4$. This comparison indicates that the evolution with $M = 0$ only associates with the minimization of interfacial curvature. A large value of penalty parameter is necessary to approximately preserve the surface area.

4.4. Two-phase vesicles with various initial shapes

In this subsection, we investigate the dynamic deformation of two-component vesicles by setting different initial shapes. The initial values of velocity field and pressure are zero. The initial conditions of six cases are defined in

Appendix. In this test, the reason of setting different initial shapes is to investigate the dynamic deformations under the combined effects of elastic bending, area-conservation constraint, and adhesion potential. In a recent work, Hu et al. [46] observed different evolutionary dynamics by defining various initial shapes for Willmore flow. We use $\Delta t = 0.01$ and mesh size 128×128 to perform the simulations. In Fig. 7, the evolutions of area ratio with respect to different initial states are plotted. The insets display the snapshots of two vesicles at different moments. Due to the effect of adhesion potential, the vesicles eventually adhere to each other. In these processes, the conservation of surface area is approximately satisfied. During early stages of cases 1–5 in Fig. 7, the membranes evolve in time. Thus, we can observe the slight fluctuation of relative errors, even though the errors are relatively small. In the late stages of cases 1–5, we observe that the curves of relative errors become approximately flat and the changes of membranes are not clear. The results indicate that the curve of relative error can be used as an indicator to judge if a membrane reaches the steady state. Because the initial shapes in case 6 are irregular, this case might need a relatively long time to reach the steady state. Therefore, we find that the curves of relative errors do not become flat in the same time range.

In Fig. 8(a) and (b), the original energy and the corrected energy with respect to different cases are plotted. It can be observed that the energy dissipation laws are satisfied for each case. In Fig. 8(c), we draw the evolutions of difference between the original and modified energies, i.e., $|E_O^n - E_M^n|$. The differences between the original and corrected energies are not plotted because they are within the limits of machine error. The evolutions of Q are plotted in Fig. 8(d), the results indicate the good consistency for each case. Because the modified energy and the original energy are not consistent, the obvious drop of energy at early stage will lead to the increase of difference between the original and modified energy values. Therefore, larger values of error can be observed at early stages. As time evolves, the energy changes become more stable, which leads to a reduction of errors during the later stages.

## 4.5. Two-components vesicles under shear flow

Shear flow is a typical fluid environment for investigating the dynamic deformation of vesicles. Under the effects of shear forces and low Reynolds numbers, vesicles undergo tank-treading deformations [7]. This flow-driven deformation is useful in drug transportation due to the changes of interfacial dynamics. Relevant numerical simulations and real experiment validations can be found in [47,48]. In this subsection, the deformation of two vesicles in shear flow is simulated. On the top and bottom boundaries, the velocity boundary conditions are set to be

$$u|_{y=0} = -U, \quad u|_{y=2\pi} = U, \quad v|_{y=0} = v|_{y=2\pi} = 0.$$

The initial conditions are defined in Appendix. We use $\Delta t = 0.01$, $U = 0.1$, and the mesh size 128×128. The snapshots of shear flow-driven deformation of vesicles are shown in Fig. 9. The interfaces are represented by the zero level-set of ϕ_i $(i = 1, 2)$. At each specific moment, the streamline is also plotted. Under the combined effects of shear flow and adhesion potential, we observe that the two vesicles are elongated but always adhered together. In the bottom row of Fig. 9, the evolutions of surface area ratios are plotted. It can be observed that the surface areas are approximately conserved. In this test, the two vesicles are symmetric with respect to the central point of the domain. Due to the same fluid parameters and the symmetric distribution of surface tension, a vortex appears in the central position following the adhesion of the two vesicles.

4.6. Three-phase vesicles with various initial shapes

In this subsection, we investigate the dynamic deformation of three-component vesicles by setting four different initial shapes. The initial velocities and pressure are zero. The initial conditions of four cases are defined in Appendix. In the simulations, we use $\Delta t = 0.01$ and the mesh size 128×128. The evolutions of surface area ratios with respect to different cases are plotted in Fig. 10. In each figure, the insets show the evolutionary snapshots of vesicles. Under the effect of adhesion forces, it can be observed that the vesicles are adhered together. Comparing these three-phase cases to the two-phase cases in Section 4.4, we see the three-phase evolutions are delayed because the dynamic deformation of one vesicle is affected by the other two vesicles. In same time range, the curves of relative errors do not become flat in most cases. In case 1, the setting is similar with case 3 in
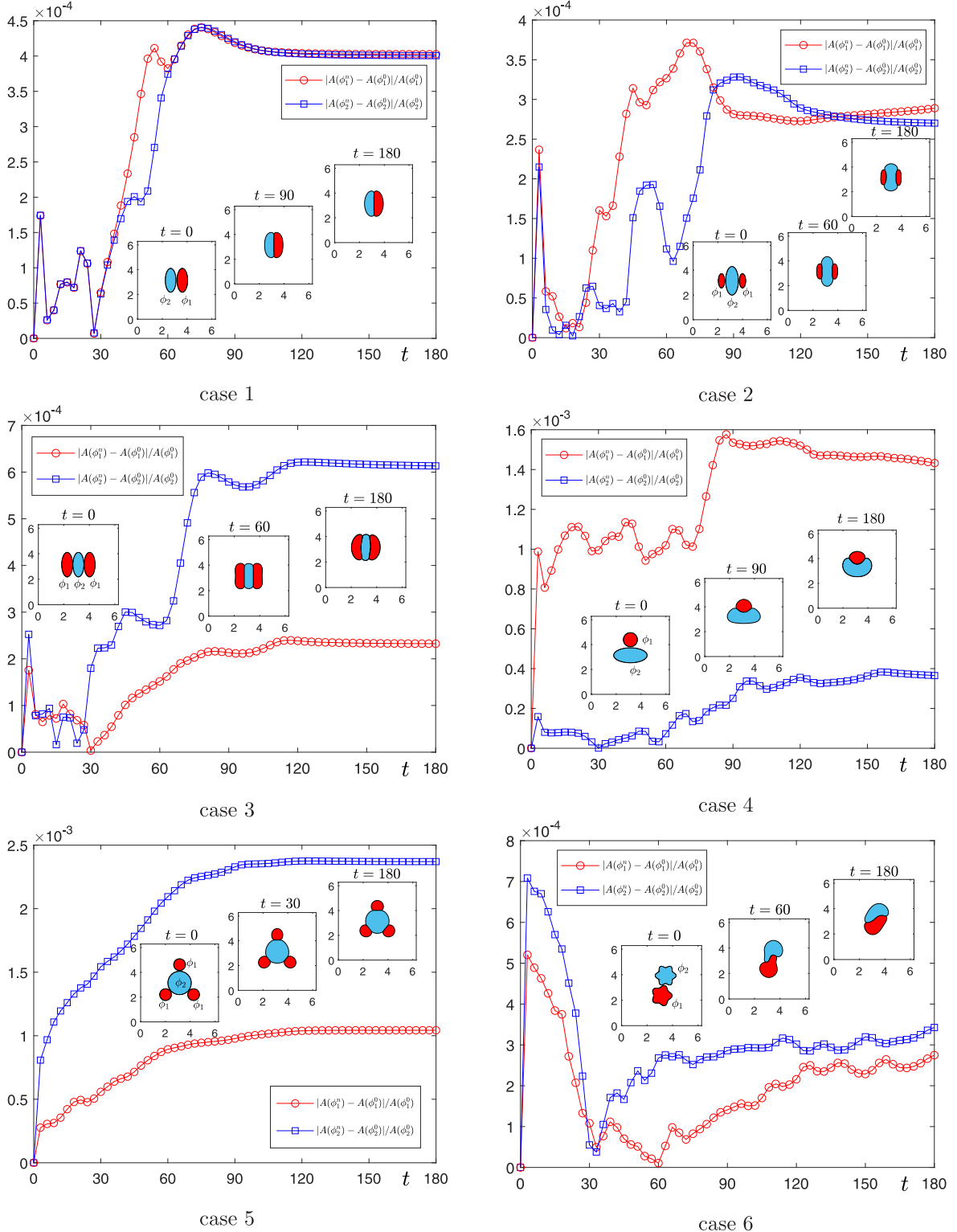
Fig. 7. Dynamic deformation of two vesicles. In each case, the evolutions of area ratio are plotted. The insets show the snapshots at different moments.
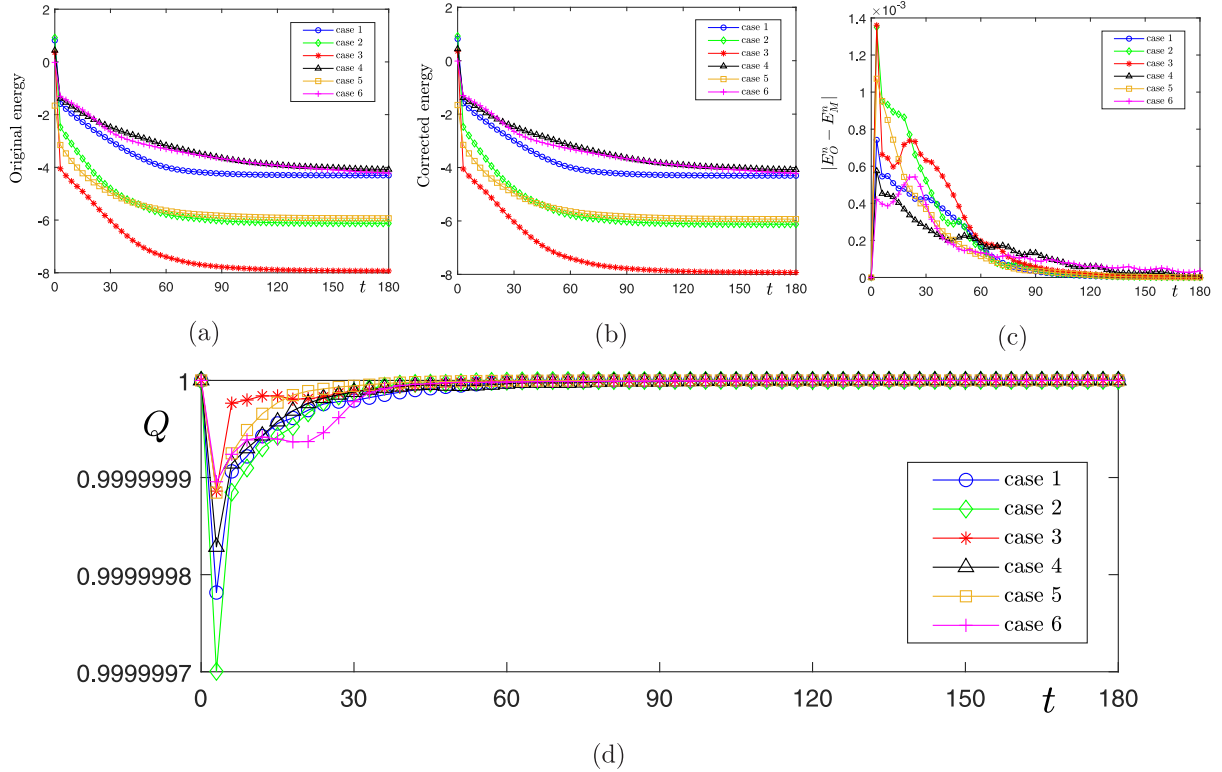
Fig. 8. Evolutions of original energy, corrected energy, and differences between original energy and modified energy are shown in (a), (b), and (c). The evolutions of Q are plotted in (d).

Section 4.4. Moreover, ϕ_1 is only affected by ϕ_3, vice versa. Thus, we observe that the curves of relative errors become approximately flat at late stage.

We plot the original energy curves and the corrected energy curves in Fig. 11(a) and (b). In Fig. 11(c), the difference between the original energy and the modified energy is shown. The differences between the original energy and the corrected energy are not plotted because they are within the limits of machine error. The energy curves are decreasing for different cases. The results plotted in Fig. 11(d) show that Q is close to 1.

4.7. Three vesicles under shear flow

In this numerical example, we simulate the shear flow-driven deformations of three-component vesicles. The velocity boundary conditions keep unchanged like those in Section 4.5. For the definitions of two initial conditions, see Appendix. The evolutions with respect to the two cases are shown in Figs. 12 and 13. The initial arrangements lead to different distribution of surface tension in space. Then, the resulting streamlines are totally different. Due to the combined effects of adhesion force and shear flow, three vesicles are elongated and adhered. The results plotted in Fig. 14(a) and (b) indicate that the surface areas with respect to the two cases are approximately conserved. For case 1, three vesicles are symmetric with respect to the central point of the domain. Due to the symmetric distribution of surface tension, a vortex can be observed in the central position (i.e., the region occupied by ϕ_2). In case 2, three vesicles are not symmetric with respect to the central point of the domain. Therefore, this asymmetric distribution of surface tension leads to the formation of vortex at the rear of second vesicle.

4.8. Multiple vesicles in arbitrary domains

In biological fluid engineering, the lipid vesicles are generally restricted into irregular regions, such as the micro-fluid devices and the wavy blood vessels. Park et al. [49] investigated the transient dynamics of an elastic capsule
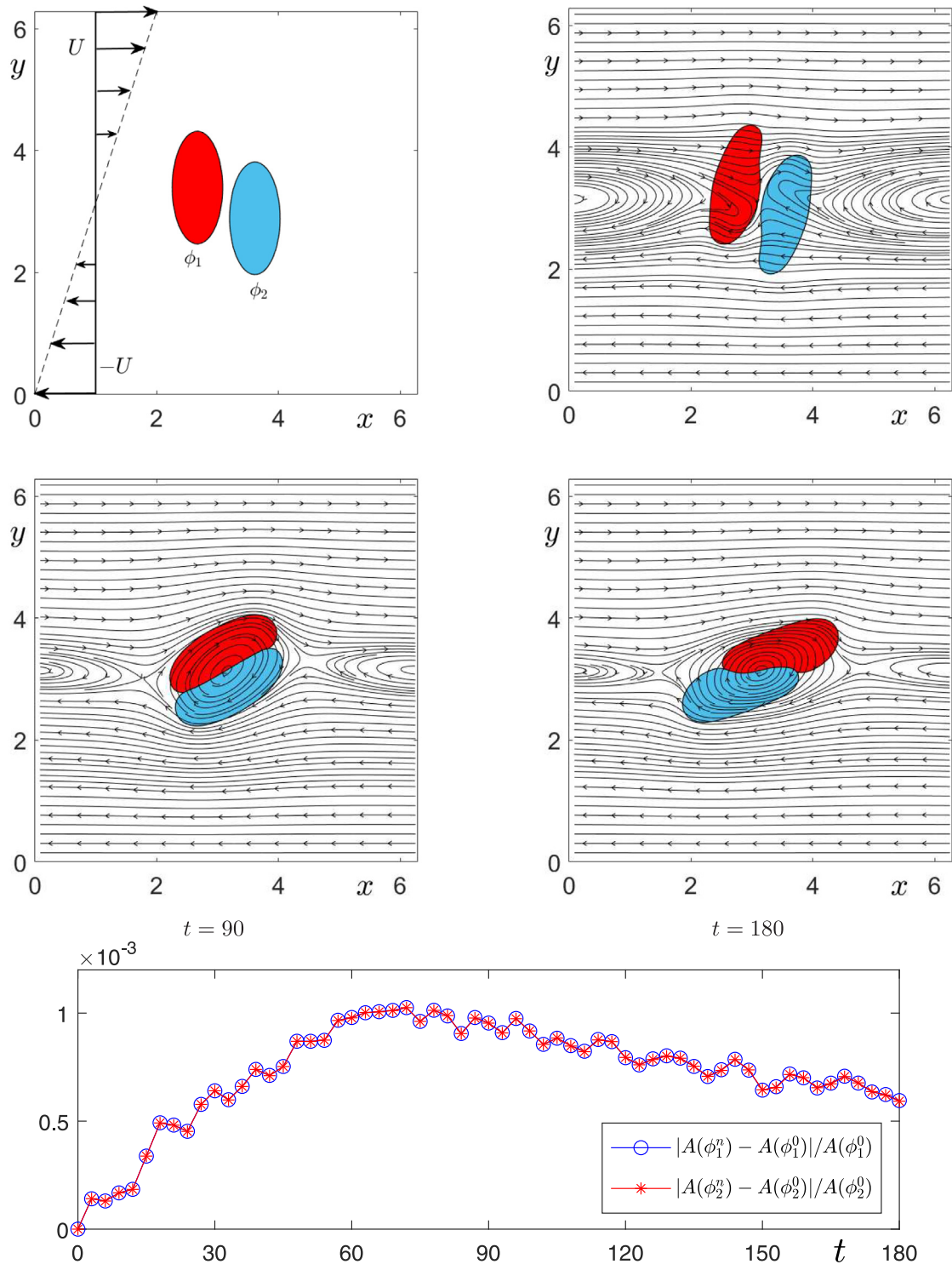
Fig. 9. Dynamic deformations of two vesicles in shear flow. The computational moments are illustrated under each figure. The evolutions of surface area ratios are shown in the bottom row.

case 1

case 2

case 3

case 4
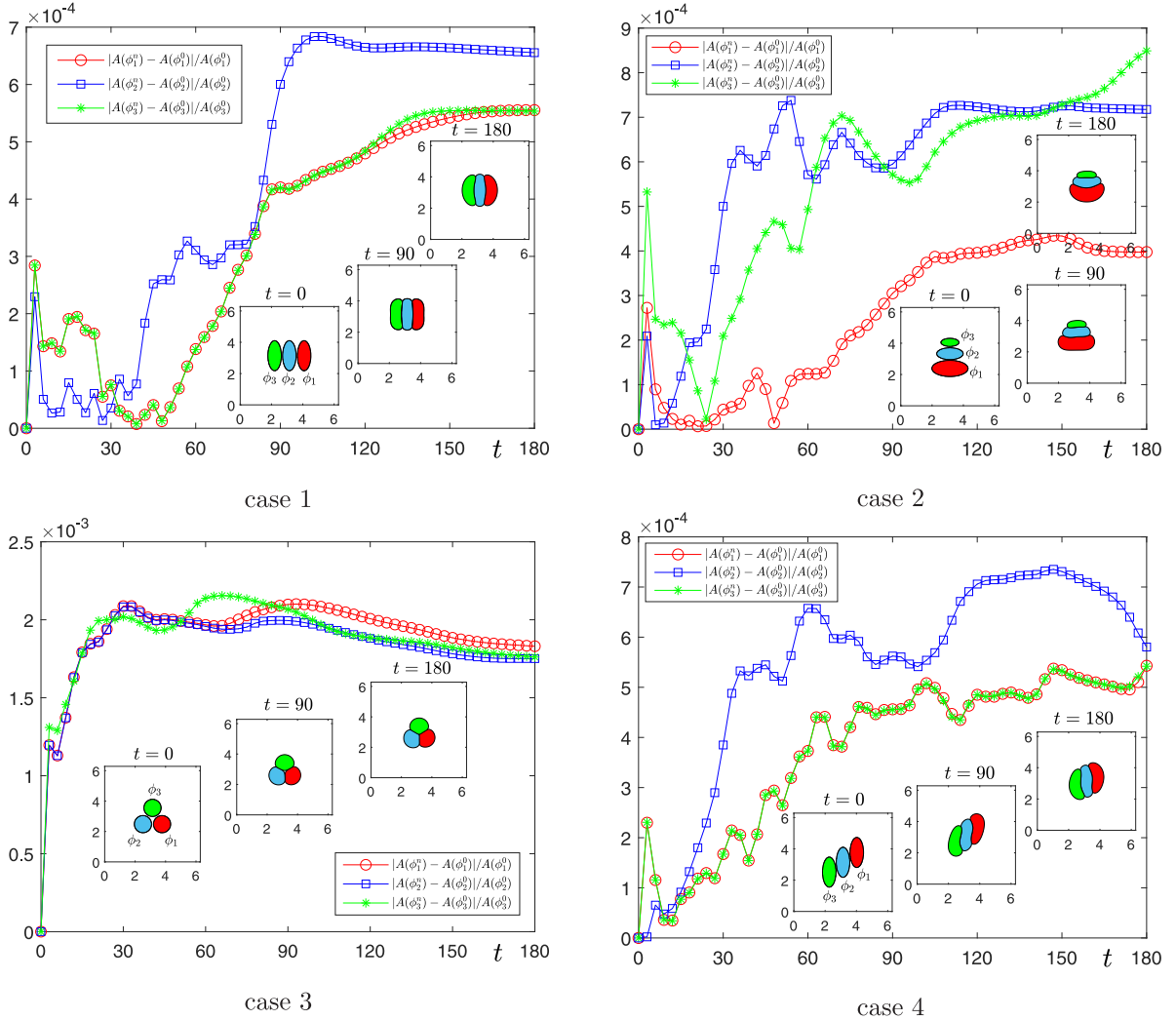
Fig. 10. Dynamic deformation of three vesicles. In each case, the evolutions of area ratio are plotted. The insets show the snapshots at different moments.

in a constricted micro-fluid channel. Ye et al. [50] performed numerical simulation of red blood cells in a 3D tube. Recently, Ye et al. [51] numerically designed a microfluidic chip for the red blood cells. To test the performance of our proposed method in these fluid environments, we recast the governing equations into the following forms

$$\frac{\partial \phi_i}{\partial t} + \nabla \cdot (\boldsymbol{u} \phi_i (1 - \Psi)) = -\gamma (\mu_i - \beta_i), \quad i = 1, 2, \ldots, N, \tag{46}$$

$$\mu_i = \lambda(\epsilon(\Delta - f'(\phi_i))(\Delta \phi_i - f(\phi_i)) + \epsilon M(A(\phi_i) - B_i)(-\Delta \phi_i + f(\phi_i))) - \sum_{j=1, j \neq i}^{N} C_{ij} \phi_i (\phi_j^2 - 1), \tag{47}$$

$$\frac{\partial \boldsymbol{u}}{\partial t} + \boldsymbol{u} \cdot \nabla \boldsymbol{u} = -\nabla p + \frac{1}{Re} \Delta \boldsymbol{u} - \sum_{i=1}^{N} \phi_i \nabla \mu_i + \frac{\Psi}{\zeta} (\boldsymbol{u}_s - \boldsymbol{u}), \tag{48}$$

$$\nabla \cdot \boldsymbol{u} = 0, \tag{49}$$

where Ψ is an indicator function. In solid and fluid, we set $\Psi = 1$ and 0, respectively. The velocity of solid is $\boldsymbol{u}_s$ and we let $\boldsymbol{u}_s = 0$ to model the incompressible fluid flows past a fixed solid [52]. Here, $\zeta > 0$ is a sufficiently small
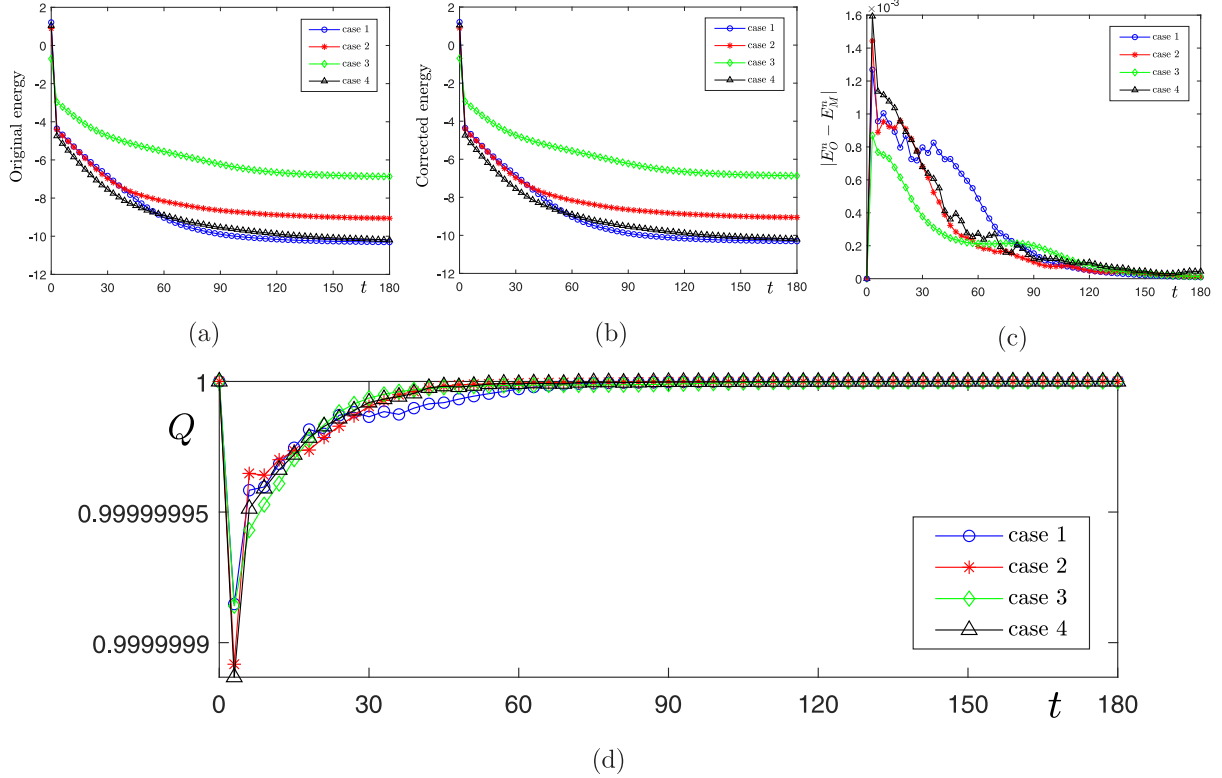
Fig. 11. Evolutions of original energy, corrected energy, and differences between original energy and modified energy are shown in (a), (b), and (c). The evolutions of Q are plotted in (d).

constant to reflect the permeability. The first simulation in this subsection is performed in $\Omega = (0, 4\pi) \times (0, 2\pi)$. We define the values of Ψ of a restricted channel as follows

$$\Psi(x, y) = \begin{cases} 1 & \text{if } x \in [1.3\pi, 2.7\pi] \text{ and } y > 1.4\pi, \\ 1 & \text{if } x \in [1.3\pi, 2.7\pi] \text{ and } y < 0.6\pi, \\ 0 & \text{otherwise.} \end{cases}$$

On the top and bottom boundaries, the velocities are set to be zero. The inlet and outlet boundary conditions are imposed on the left and right boundaries, respectively. The inlet velocity $u = 0.01 \sin(0.5y)$ is adopted. For the scalar variables, i.e., ϕ_i and p, the zero-Neumann boundary condition is used on all boundaries. We set $\zeta = 1e-8$. The mesh size 256×128 and the time step $\Delta t = 0.01$ are used to perform the computation. The initial conditions are defined in Appendix. Fig. 15 displays the snapshots of the three vesicles past through a restricted channel at different moments. The associated streamlines are also plotted. Under the effect of restricted flow field, the dynamic deformations can be observed. Due to the adhesion force, three vesicles are adhered all along. In Fig. 16(a) and (b), we plot the evolutions of the surface area ratios and Q, respectively.

In this test, we observe that $M = 1e4$ leads to the desired conservation of surface area. Therefore, the increase of M might not lead to the formation of parachute-like shapes of vesicles. Because the phase-field vesicle model is sensitive to interfacial parameters, we herein perform the simulation with $\epsilon = 0.05$ and mesh size 512×256. In present mesh size, $\epsilon = 0.05$ represents that the diffuse interface occupies more grids, see [53] for the relationship between ϵ and mesh grid. To reduce the mobility, we choose $\lambda = 1e-4$. In Fig. 17, the snapshots at specific moments are shown. When the vesicles flow through the restricted channel, they evolve to parachute-like shapes.

In the second simulation, we consider three vesicles flowing through a micro-vessel stenosis [54]. The full domain is $\Omega = (0, 4\pi) \times (0, 2\pi)$. The initial conditions of three vesicles are defined in Appendix. The inlet velocity is defined as $u = 0.01 \sin(0.5y)$. We use $\Delta t = 0.01$, $\zeta = 1e-8$, $\lambda = 1e-3$, and mesh size 256×128. The snapshots of interfacial profiles (i.e., $\phi_i = 0$ $(i = 1, 2, 3)$) and streamline at different moments are displayed in Fig. 18. Because
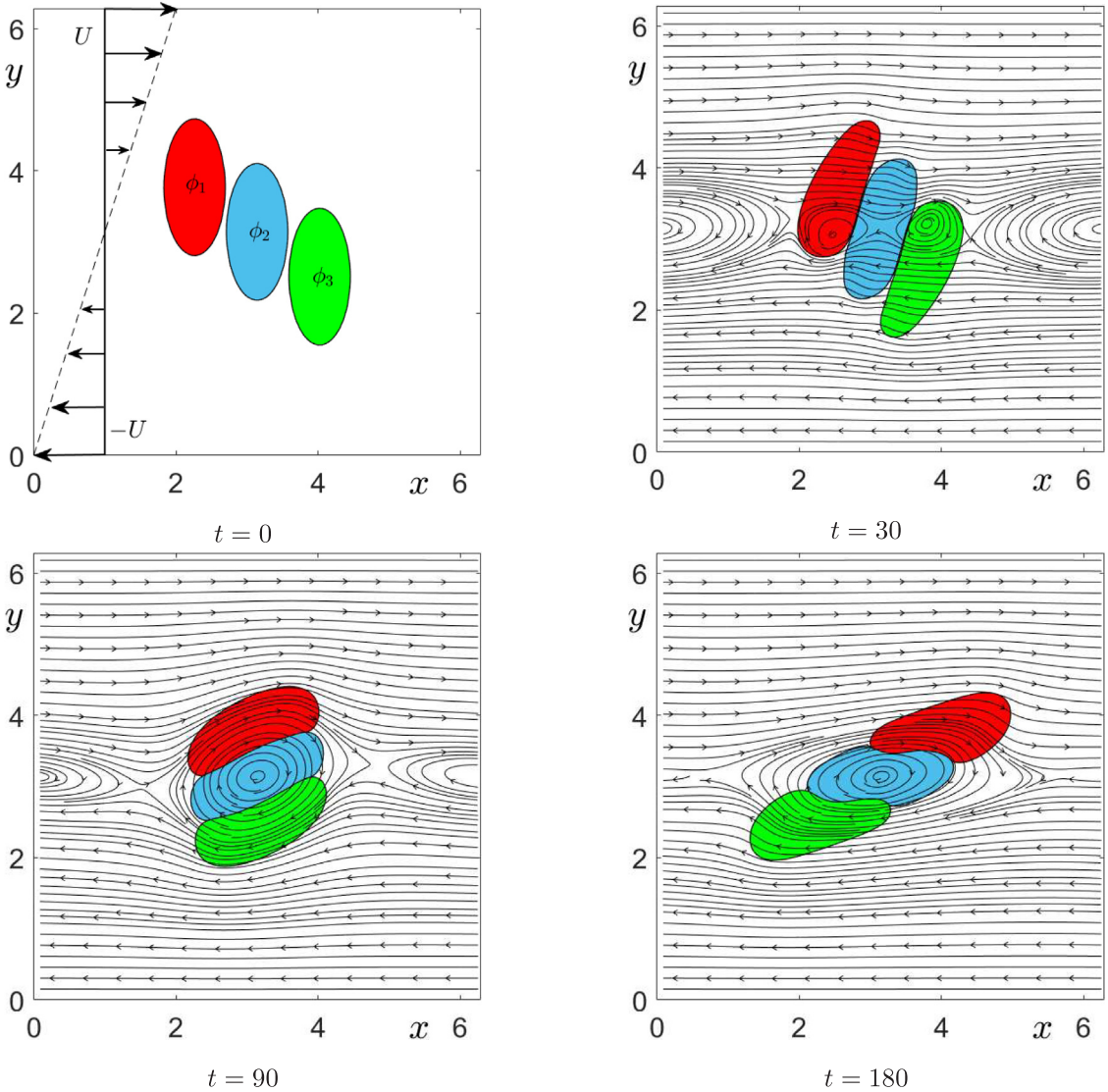
Fig. 12. Dynamic deformations of three vesicles (case 1) in shear flow. The computational moments are illustrated under each figure.

the vesicles represented by ϕ_2 and ϕ_3 are adhered together, the evolutionary dynamics in narrow channel is delayed. We can observe that the vesicle represented by ϕ_1 fast flows through the channel. In the late stage, three vesicles are adhered to each other because of the effect of adhesion force. The evolution of Q is plotted in the bottom row of Fig. 18. When fluid flows through the narrow channel, the velocity at the left inlet will become fast. The first vesicle (i.e., ϕ_1) are fast convected into the channel. The last two vesicles adhere together and simultaneously flow through the narrow channel, their velocity cannot be faster than that of the first vesicle. Therefore, we observe that ϕ_2 and ϕ_3 always locate behind ϕ_1 in the narrow channel.

It is worth noting that the membrane of a vesicle is only mathematically represented by the zero level-set of ϕ_i, the diffuse interface still has a measurable thickness. Although the penalty term $-\sum_{j=1, j\neq i}^{N} C_{ij}\phi_i(\phi_j^2 - 1)$ can prevent the obvious penetration of ϕ_i into ϕ_j in their bulk phases (i.e., $\phi_i = 1$ and $\phi_j = 1$), the interfacial motion inside the diffuse interface region will lead to the overlap between $\phi_i = 0$ and $\phi_j = 0$ ($i \neq j$). When the advection is not dominant or the system is in steady state, we can expect the zero level-set of each vesicle intersects at a same position. Fig. 19(a) and (b) schematically illustrates the 1D profiles of two vesicles in equilibrium state and in advection-dominated environment, respectively. This explains why the overlaps at specific moments can be observe
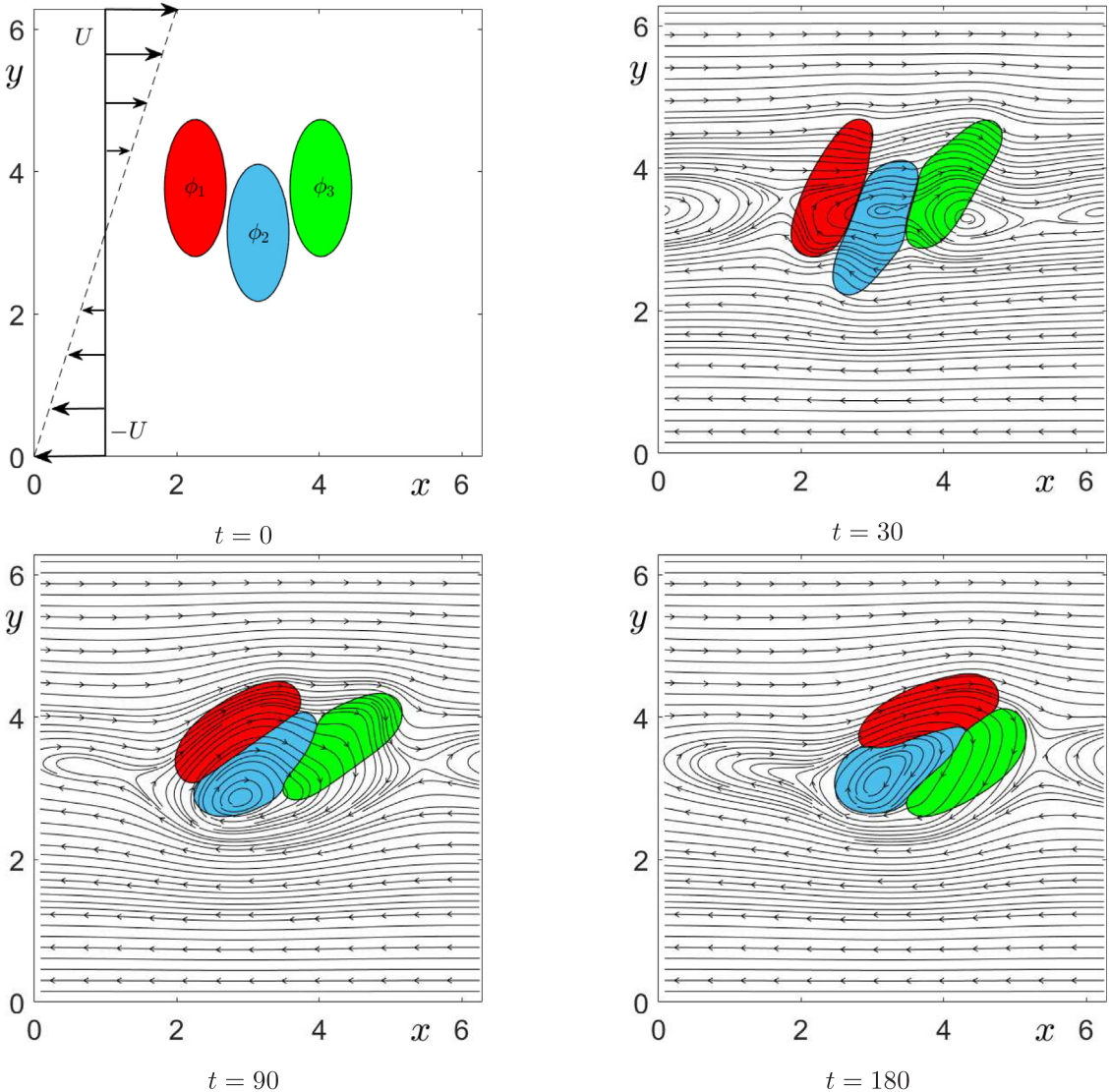
Fig. 13. Dynamic deformations of three vesicles (case 2) in shear flow. The computational moments are illustrated under each figure.

in Fig. 18. A natural approach for reducing overlap is to refine the mesh grid. Fig. 20 shows the results with mesh size 512×256. With a finer mesh size, the thickness of diffuse interface becomes thinner. Therefore, we do not observe the obvious overlap between ϕ_2 and ϕ_3.

The last example in this subsection aims to simulate the four-component vesicles flowing through a wavy channel. The full domain is $\Omega = (0, 4\pi) \times (0, \pi)$. The solid region is defined by using the following two functions in $x \in [0.2\pi, 3.8\pi]$

$$y = 0.2\sqrt{x/\pi} \sin(3x) + 0.75\pi, \quad y = 0.04(x/\pi)^2 \cos(2x) - 0.08 \sin(8x) + 0.3\pi.$$

The initial conditions of four adjacent vesicles are defined in Appendix. Fig. 21 shows the dynamic deformations at different moments. Due to the adhesion force, four vesicles are closely adhered. The evolution of Q is plotted in the bottom row of Fig. 21. When the vesicles flows through the narrowest region, we observe that the difference between Q and 1 becomes slightly large. In numerical computation, the update of Q relies on the energy relationship. We note that the energy dissipation law cannot strictly hold for the tests of vesicles flowing through complex channels because of the effects of inlet and outlet boundaries. Moreover, the numerical energy can also be affected in the
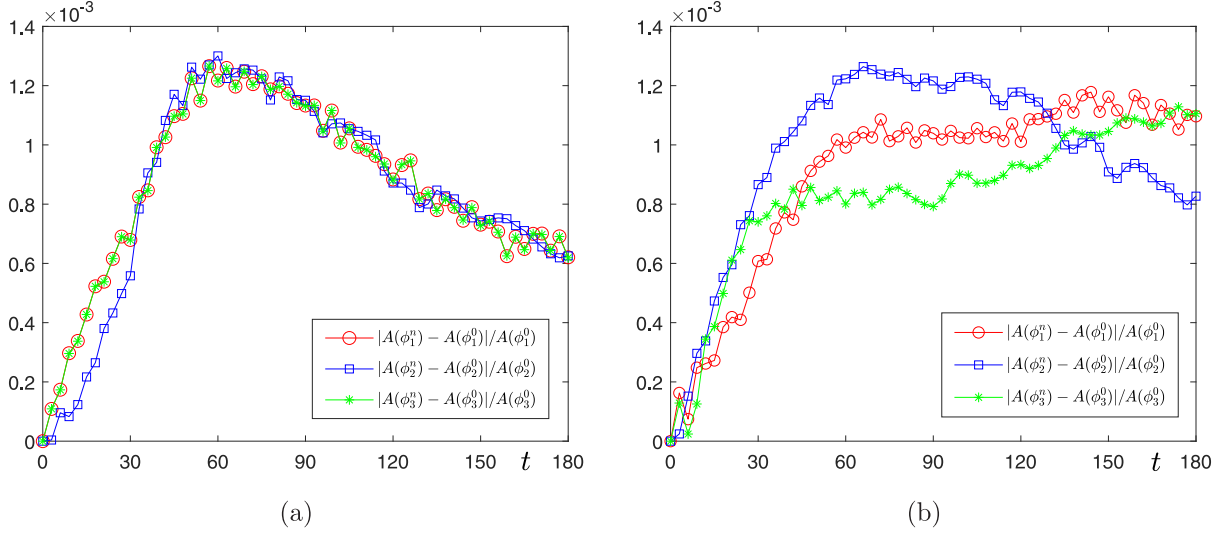
Fig. 14. Evolutions of surface area ratios with respect to (a) case 1 and (b) case 2.

region where fluid velocity changes fast, which leads to a noticeable decrease in the numerical value of Q. During the whole process, the consistency is still satisfactory because Q is close to 1. It is worth noting that the inlet velocity used in this test is small. Moreover, the initial circular shapes correspond to the minimization state of elastic bending energy. Thus, we find that the vesicles do not undergo large deformations in the channel.

4.9. Fluid flow-coupled vesicles in 3D spaces

Finally, we conduct three simulations in 3D spaces to further show the performance of our method. In the first simulation, we consider the deformation of two vesicles with the absence of external fluid flow. The 3D space is $\Omega = (0, \pi) \times (0, \pi) \times (0, \pi)$. Along x- and y-directions, all variables are periodic. On the top and bottom boundaries, the zero-Neumann and no-slip boundary conditions are imposed on scalar variables and velocities, respectively. The parameters are set to be $\Delta t = 0.01$, $\epsilon = 0.065$, and $\lambda = 1\mathrm{e}{-3}$. The initial conditions of two adjacent vesicles are defined in Appendix. The initial velocities and pressure are zero. From Fig. 22, it can be observed that two vesicles are gradually adhered in time. In Fig. 23(a) and (b), the evolutions of energy curves and surface area ratios are plotted. The results denote that the energy dissipation and the approximate area conservation are satisfied in 3D space.

In the second test, we investigate the dynamic deformations of two 3D adjacent vesicles in shear flow. The initial velocities are

$$u(x, y, z, 0) = U(2z/\pi - 1), \quad v(x, y, z, 0) = w(x, y, z, 0) = 0. \tag{50}$$

The initial conditions of vesicles are unchanged. On the top and bottom boundaries, the following velocity conditions are imposed

$$u|_{z=0} = -U, \quad u|_{z=\pi} = U, \quad v|_{z=0} = v|_{z=\pi} = w|_{z=0} = w|_{z=\pi} = 0.$$

Here, $U = 0.1$. Fig. 24 displays the snapshots of two vesicles in shear flow. As we can see, the vesicles are elongated and adhered together. The results plotted in Fig. 25 indicate that the surface areas are approximately conserved in time.

The last simulation focuses on the dynamic deformation and motion of 3D vesicles flowing through a restricted channel. The full domain size is $\Omega = (0, 2\pi) \times (0, \pi) \times (0, \pi)$. The same parameters in the previous two 3D simulations are used. The solid region is represented by the following indicator function

$$\Psi(x, y, z) = \begin{cases} 1 & \text{if } x \in [0.5\pi, 1.5\pi] \text{ and } z > 0.7\pi, \\ 1 & \text{if } x \in [0.5\pi, 1.5\pi] \text{ and } z < 0.3\pi, \\ 0 & \text{otherwise.} \end{cases}$$
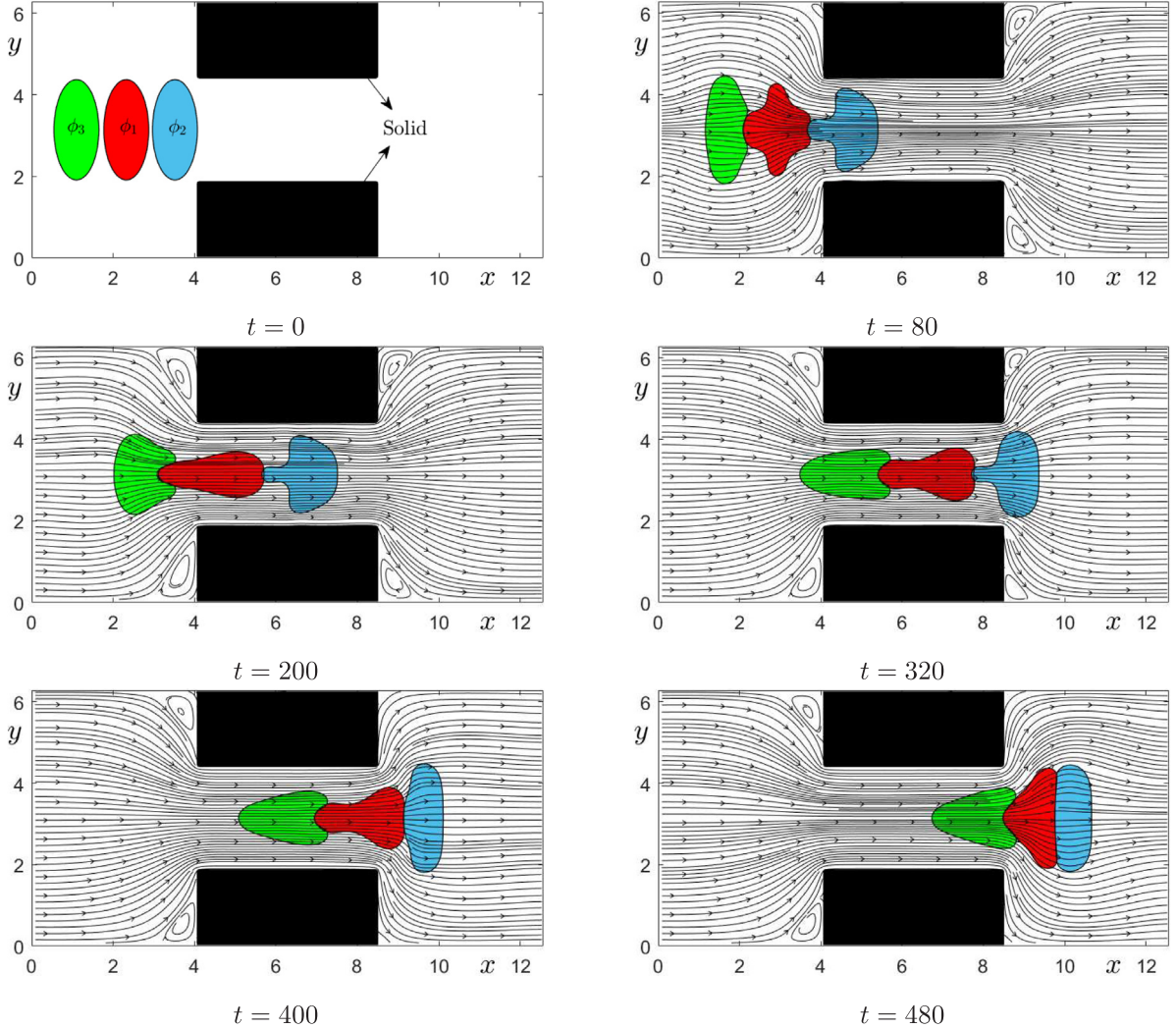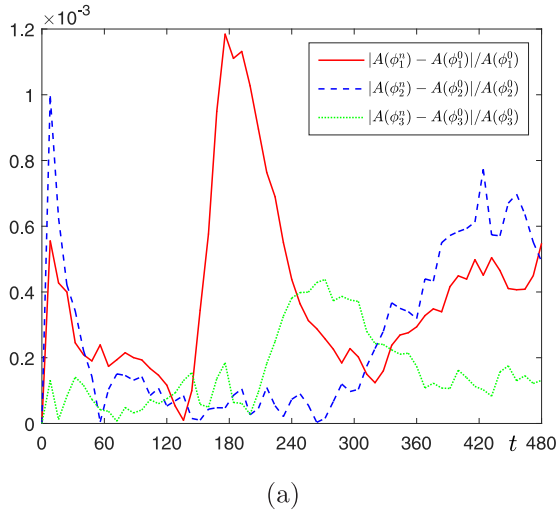
Fig. 15. Dynamic deformations of three vesicles in a restricted channel. The computational moments are illustrated under each figure.
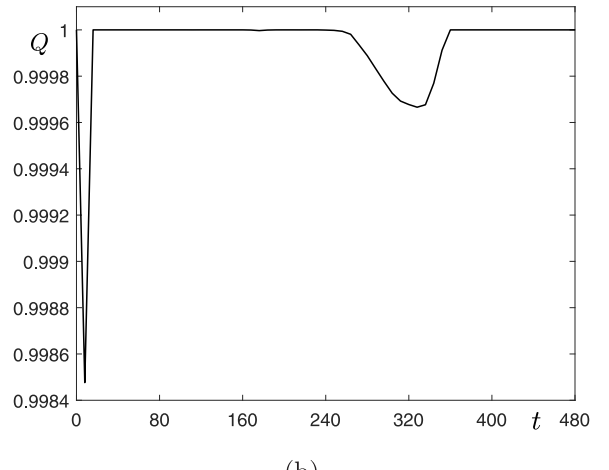
The left and right boundaries are the inlet and outlet boundaries for velocities. On the top and bottom boundaries, all velocity components are zero. The zero-Neumann boundary condition is imposed for ϕ_i ($i = 1, 2$) and p on all boundaries. The inlet velocity is defined as $u = 0.01 \sin(y) \sin(z)$. The initial conditions of two vesicles are defined in Appendix. The snapshots of vesicles at different computational moments are shown in Fig. 26. After the vesicles flow through the narrow regions, it can be observed that the adhesion force make the two vesicles gradually adhere to each other. The results plotted in Fig. 27(a) and (b) indicate the approximate conservation of surface area and the consistency, respectively.

5. Conclusions
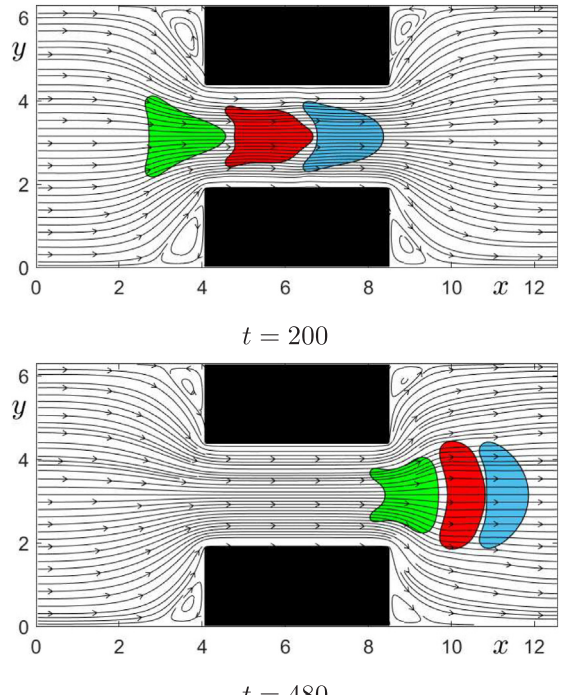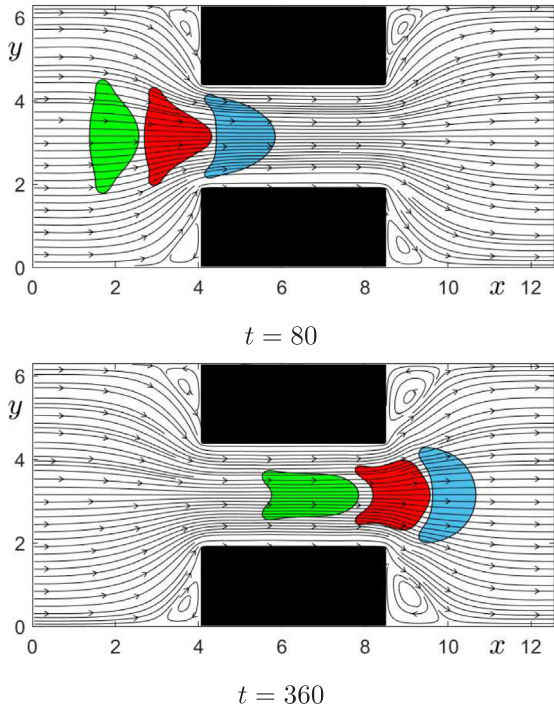
In this work, we simulated the fluid flow-coupled multiple vesicles with an incompressible NS phase-field penalty model. The time-dependent variable strategy was adopted to construct linearly decoupled and energy-stable scheme. At each time step, the solution algorithm is efficient to implement because only several linear equations needed to be separately solved. The typical benchmark tests indicated that the proposed scheme had desired energy stability and second-order accuracy in time. The capabilities of the model and algorithm were further validated via the simulations of multiple vesicles in various fluid environments.

Fig. 16. Evolutions of (a) surface area ratios and (b) Q for three vesicles past through a restricted channel.


Fig. 17. Dynamic deformations of three vesicles flowing through a restricted channel. Here, mesh size 512×256, $\epsilon = 0.05$, and $\lambda = 1e-4$ are used.
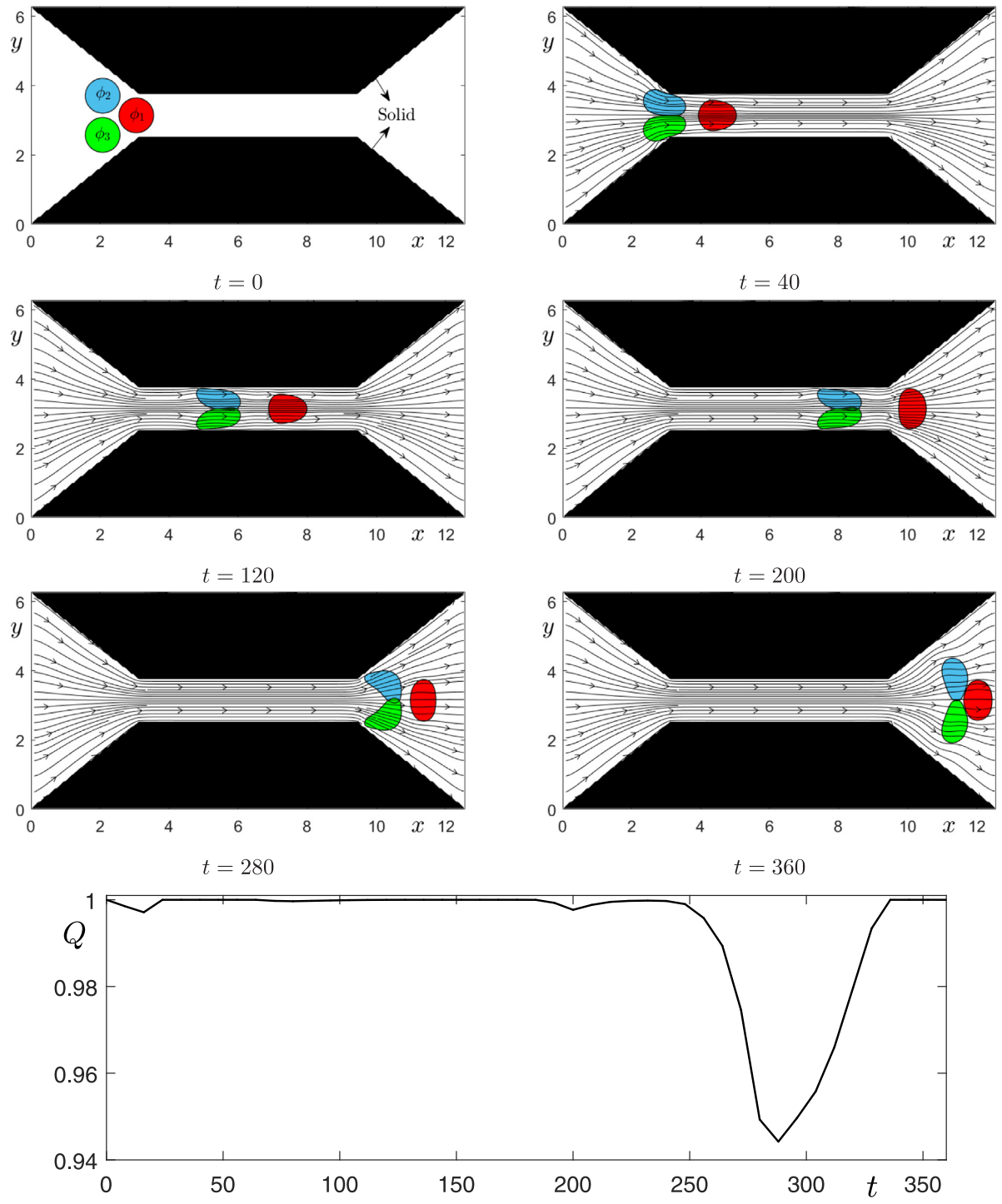
Fig. 18. Dynamic deformations of three vesicles flowing through a micro-vessel stenosis. The computational moments are illustrated under each figure. The evolution of Q is plotted in the bottom row.
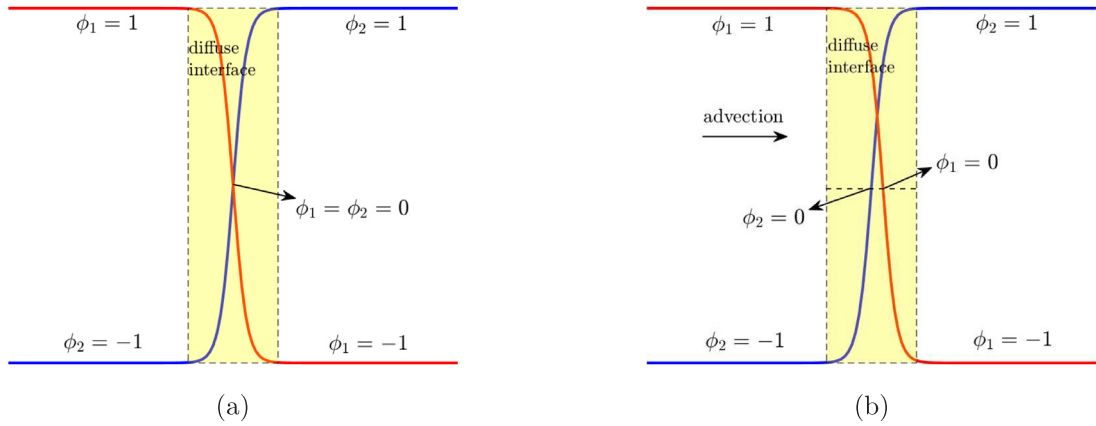
Fig. 19. Schematic illustrations of 1D profiles of two vesicles in (a) equilibrium state and in (b) advection-dominated environment. The shadow region represents the diffuse interface.
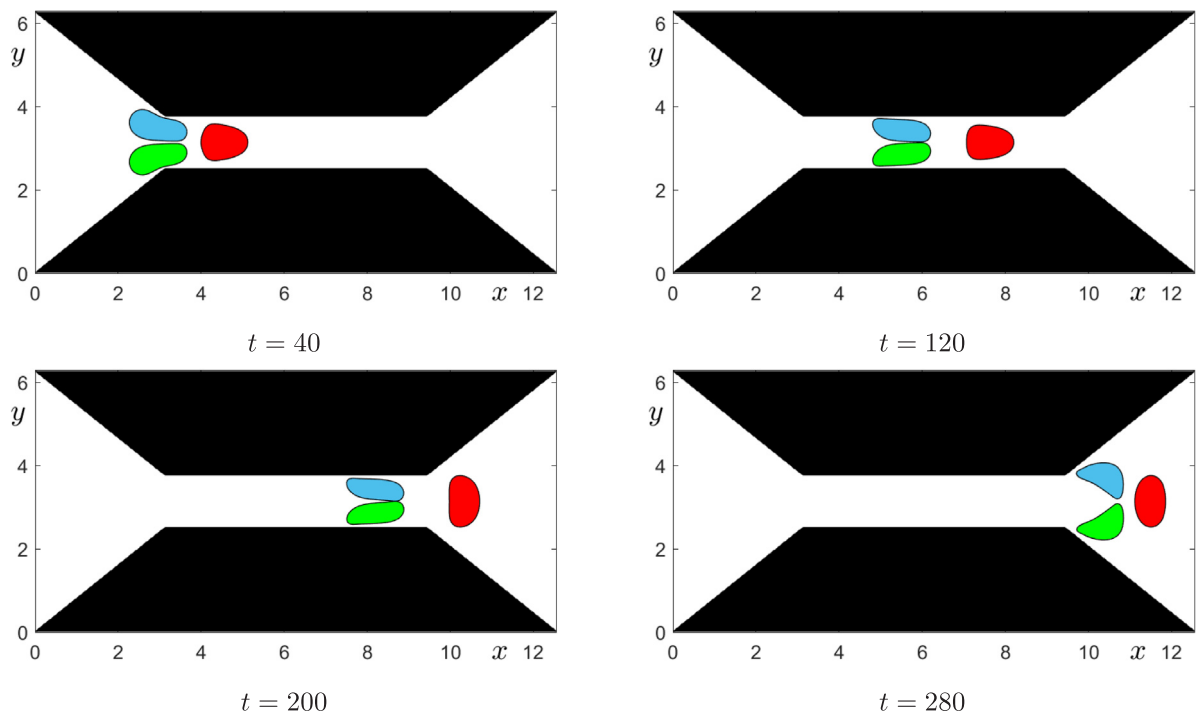
Fig. 20. Dynamic deformations of three vesicles flowing through a micro-vessel stenosis. Here, mesh size 512×256 is used.
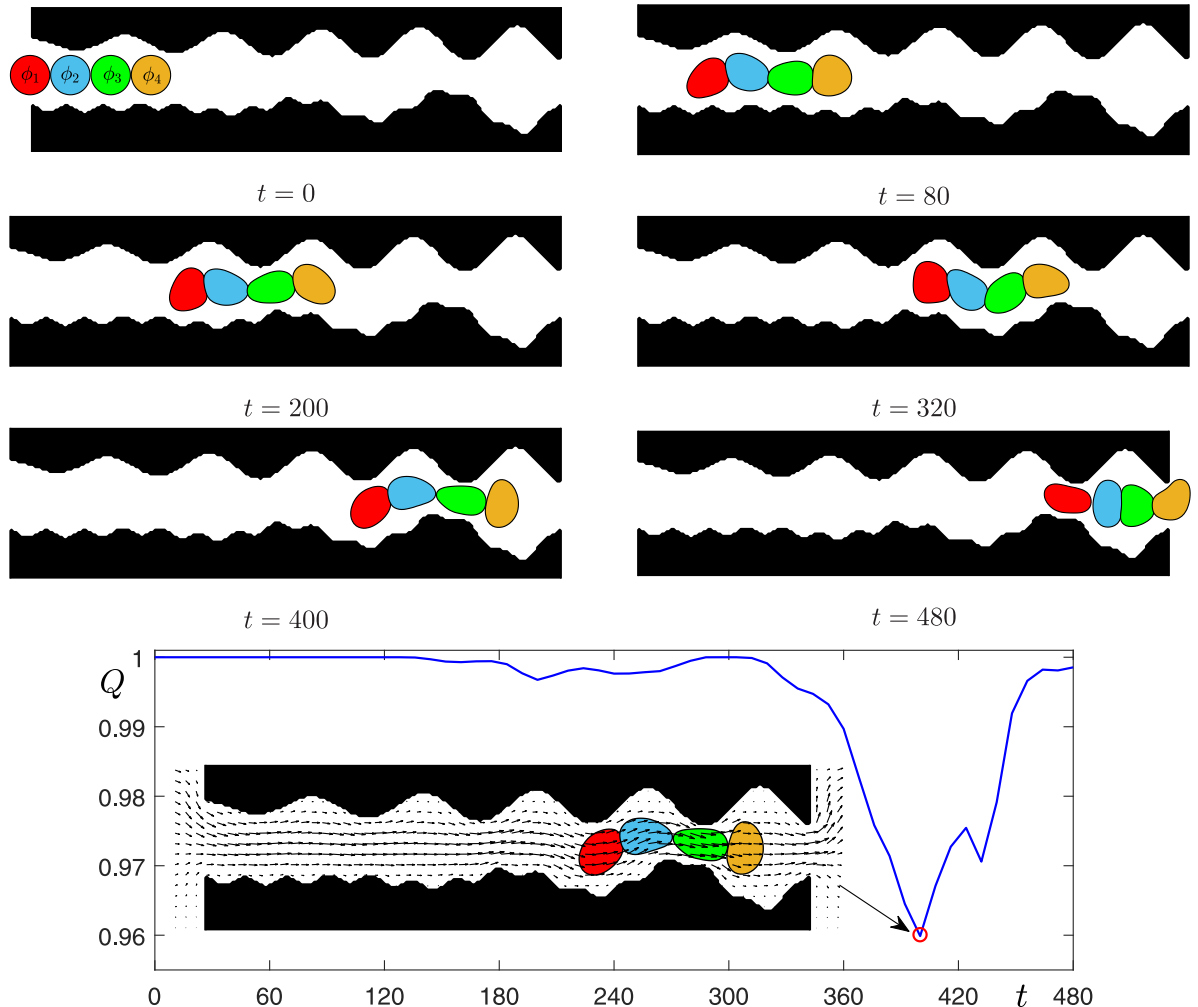
Fig. 21. Dynamic deformations of four vesicles flowing through a wavy channel. The computational moments are illustrated under each figure. The evolution of Q is plotted in the bottom row.

## Declaration of competing interest

The authors declare that they have no known competing financial interests or personal relationships that could have appeared to influence the work reported in this paper.

Data availability

Data will be made available on request.

Acknowledgments
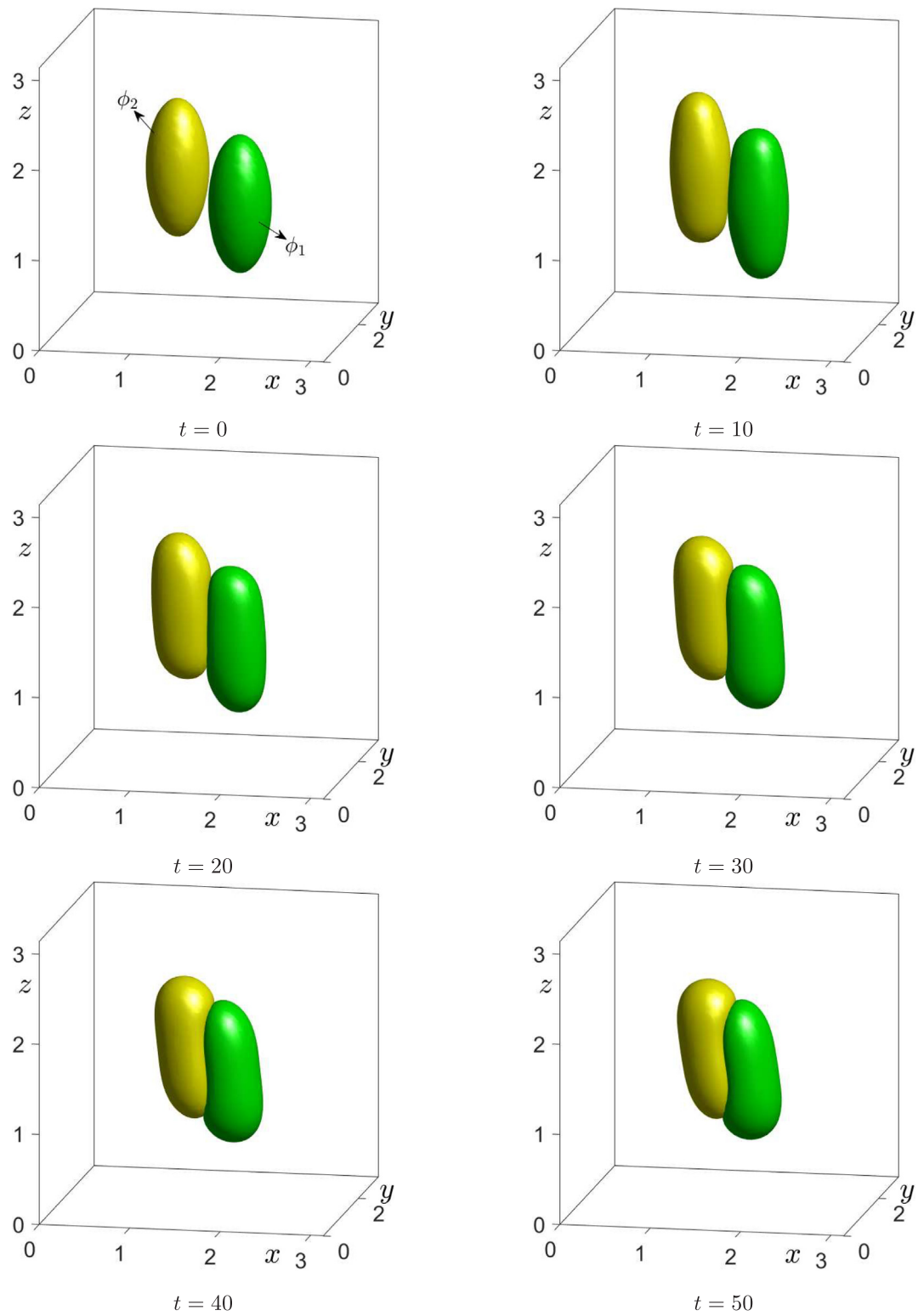
Fig. 22. Deformations of two adjacent vesicles in 3D space. Under each figure, the computational moments are illustrated.
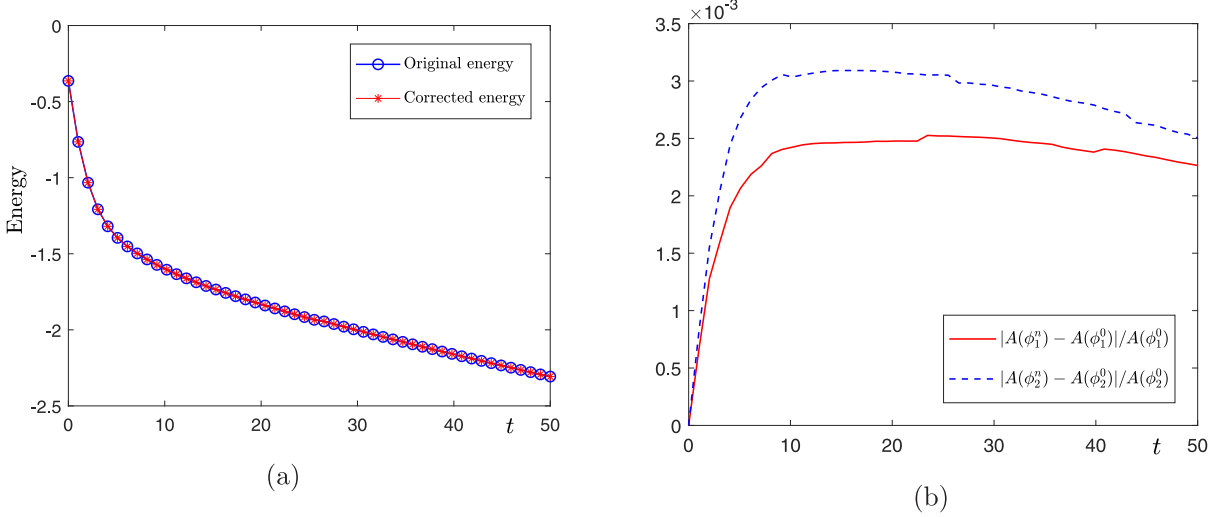
Fig. 23. Evolutions of (a) energy curves and (b) surface area ratios for two adjacent 3D vesicles.

Appendix

The initial conditions of Section 4.1 are defined as

$$\phi_1(x, y, 0) = \tanh\left(\frac{0.2\pi - \sqrt{(x - 1.22\pi)^2 + (y - \pi)^2}}{\sqrt{2}\epsilon}\right), \tag{51}$$

$$\phi_2(x, y, 0) = \tanh\left(\frac{0.2\pi - \sqrt{(x - 0.78\pi)^2 + (y - \pi)^2}}{\sqrt{2}\epsilon}\right), \tag{52}$$

$$u(x, y, 0) = v(x, y, 0) = p(x, y, 0) = 0. \tag{53}$$

The initial conditions of Section 4.3 are defined as

$$\phi_1(x, y, 0) = \tanh\left(\frac{0.25\pi - \sqrt{(x - 0.67\pi)^2/0.3 + (y - \pi)^2/1.5}}{\sqrt{2}\epsilon}\right), \tag{54}$$

$$\phi_2(x, y, 0) = \tanh\left(\frac{0.25\pi - \sqrt{(x - 1.33\pi)^2/0.3 + (y - \pi)^2/1.5}}{\sqrt{2}\epsilon}\right), \tag{55}$$

$$u(x, y, 0) = v(x, y, 0) = p(x, y, 0) = 0. \tag{56}$$

In Section 4.4, the initial conditions of six cases are defined as follows:
For the first case, we consider the following initial state of two adjacent elliptic vesicles

$$\phi_1(x, y, 0) = \tanh\left(\frac{0.25\pi - \sqrt{(x - 1.15\pi)^2/0.3 + (y - \pi)^2/1.5}}{\sqrt{2}\epsilon}\right), \tag{57}$$

$$\phi_2(x, y, 0) = \tanh\left(\frac{0.25\pi - \sqrt{(x - 0.85\pi)^2/0.3 + (y - \pi)^2/1.5}}{\sqrt{2}\epsilon}\right). \tag{58}$$

For the second case, we consider the following initial state of a big vesicle in contact with two smaller vesicles

$$\phi_1(x, y, 0) = \tanh\left(\frac{0.15\pi - \sqrt{(x - 1.27\pi)^2/0.3 + (y - \pi)^2/1.5}}{\sqrt{2}\epsilon}\right)$$
$$+ \tanh\left(\frac{0.15\pi - \sqrt{(x - 0.73\pi)^2/0.3 + (y - \pi)^2/1.5}}{\sqrt{2}\epsilon}\right), \tag{59}$$
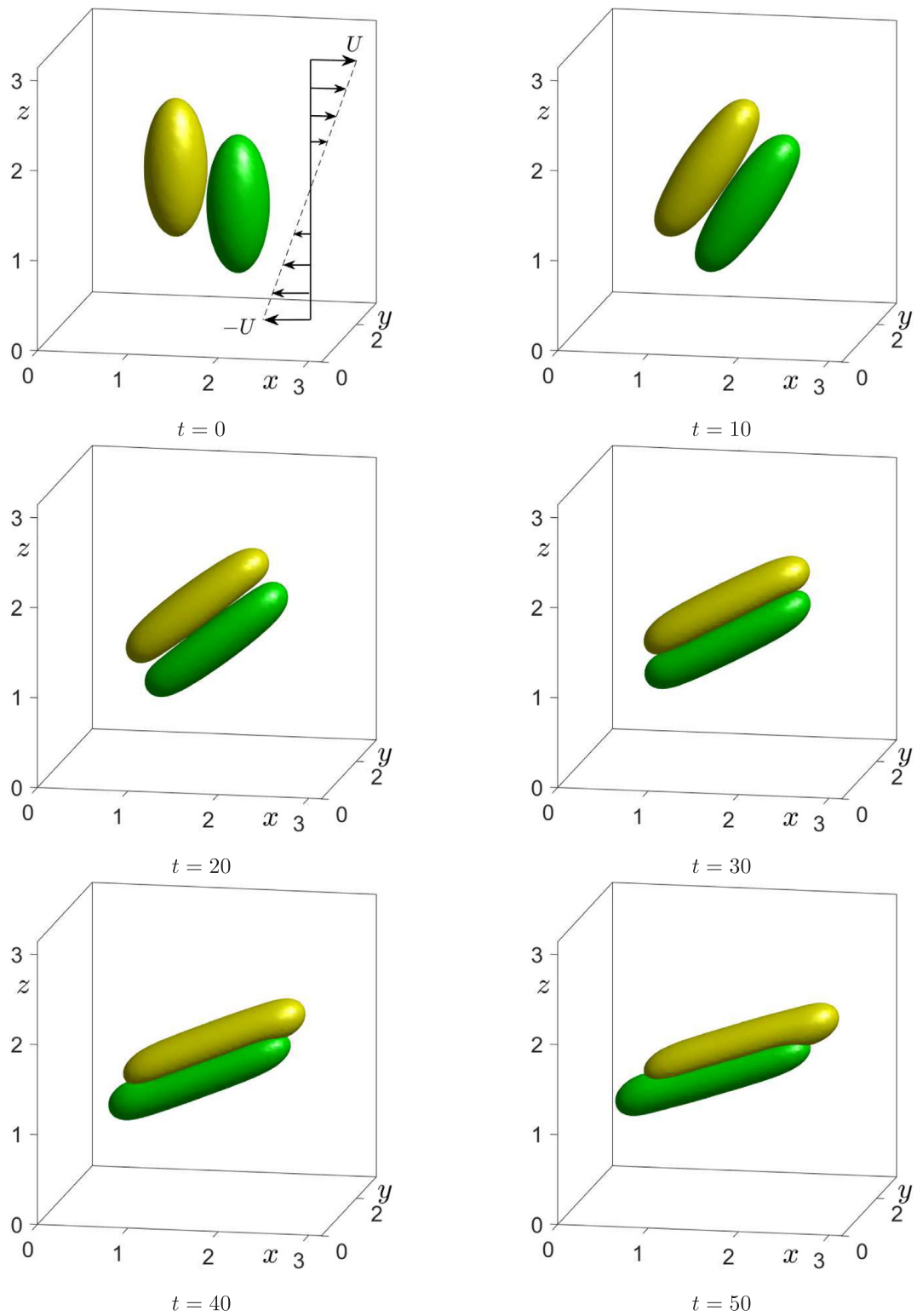
Fig. 24. Deformations of two 3D adjacent vesicles in shear flow. Under each figure, the computational moments are illustrated.
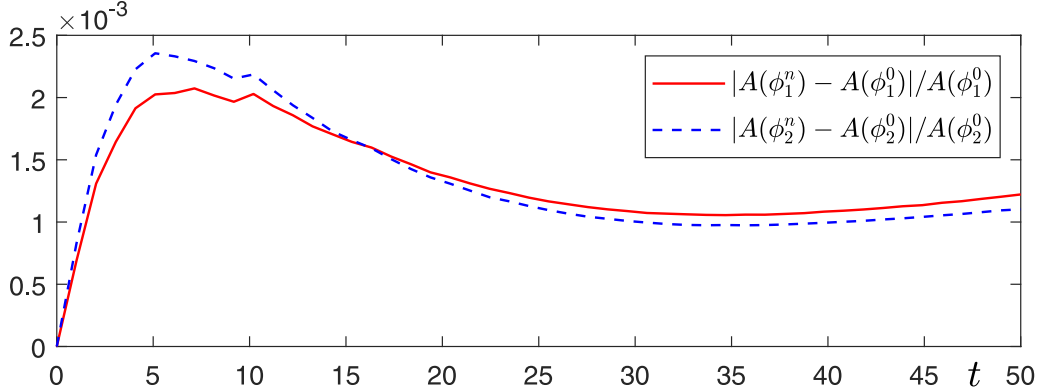
Fig. 25. Evolutions of surface area ratios for two 3D vesicles in shear flow.

$$\phi_2(x, y, 0) = \tanh\left(\frac{0.3\pi - \sqrt{(x - \pi)^2/0.3 + (y - \pi)^2/1.5}}{\sqrt{2}\epsilon}\right). \tag{60}$$

For the third case, we consider the following initial state of three elliptic vesicles with same size

$$\phi_1(x, y, 0) = \tanh\left(\frac{0.25\pi - \sqrt{(x - 1.28\pi)^2/0.3 + (y - \pi)^2/1.5}}{\sqrt{2}\epsilon}\right)$$

$$+ \tanh\left(\frac{0.25\pi - \sqrt{(x - 0.72\pi)^2/0.3 + (y - \pi)^2/1.5}}{\sqrt{2}\epsilon}\right), \tag{61}$$

$$\phi_2(x, y, 0) = \tanh\left(\frac{0.25\pi - \sqrt{(x - \pi)^2/0.3 + (y - \pi)^2/1.5}}{\sqrt{2}\epsilon}\right). \tag{62}$$

For the fourth case, we consider the following initial state of an elliptic vesicle in contact with a circular one

$$\phi_1(x, y, 0) = \tanh\left(\frac{0.18\pi - \sqrt{(x - \pi)^2 + (y - 1.4\pi)^2}}{\sqrt{2}\epsilon}\right), \tag{63}$$

$$\phi_2(x, y, 0) = \tanh\left(\frac{0.35\pi - \sqrt{(x - \pi)^2/1.5 + (y - \pi)^2/0.3}}{\sqrt{2}\epsilon}\right). \tag{64}$$

For the fifth case, we consider the following initial state of a big circular vesicle in contact with three smaller vesicles

$$\phi_1(x, y, 0) = \tanh\left(\frac{0.15\pi - \sqrt{(x - \pi)^2 + (y - 1.47\pi)^2}}{\sqrt{2}\epsilon}\right) + \tanh\left(\frac{0.15\pi - \sqrt{(x - 1.36\pi)^2 + (y - 0.7\pi)^2}}{\sqrt{2}\epsilon}\right)$$

$$+ \tanh\left(\frac{0.15\pi - \sqrt{(x - 0.64\pi)^2 + (y - 0.7\pi)^2}}{\sqrt{2}\epsilon}\right), \tag{65}$$

$$\phi_2(x, y, 0) = \tanh\left(\frac{0.3\pi - \sqrt{(x - \pi)^2 + (y - \pi)^2}}{\sqrt{2}\epsilon}\right). \tag{66}$$

For the last case, we consider the following initial state of two star-like vesicles

$$\phi_1(x, y, 0) = \tanh\left(\frac{0.23\pi + 0.1\cos(6\theta_1) - \sqrt{(x - 1.1\pi)^2 + (y - 1.25\pi)^2}}{\sqrt{2}\epsilon}\right), \tag{67}$$

$$\phi_2(x, y, 0) = \tanh\left(\frac{0.23\pi + 0.1\cos(5\theta_2) - \sqrt{(x - \pi)^2 + (y - 0.75\pi)^2}}{\sqrt{2}\epsilon}\right), \tag{68}$$
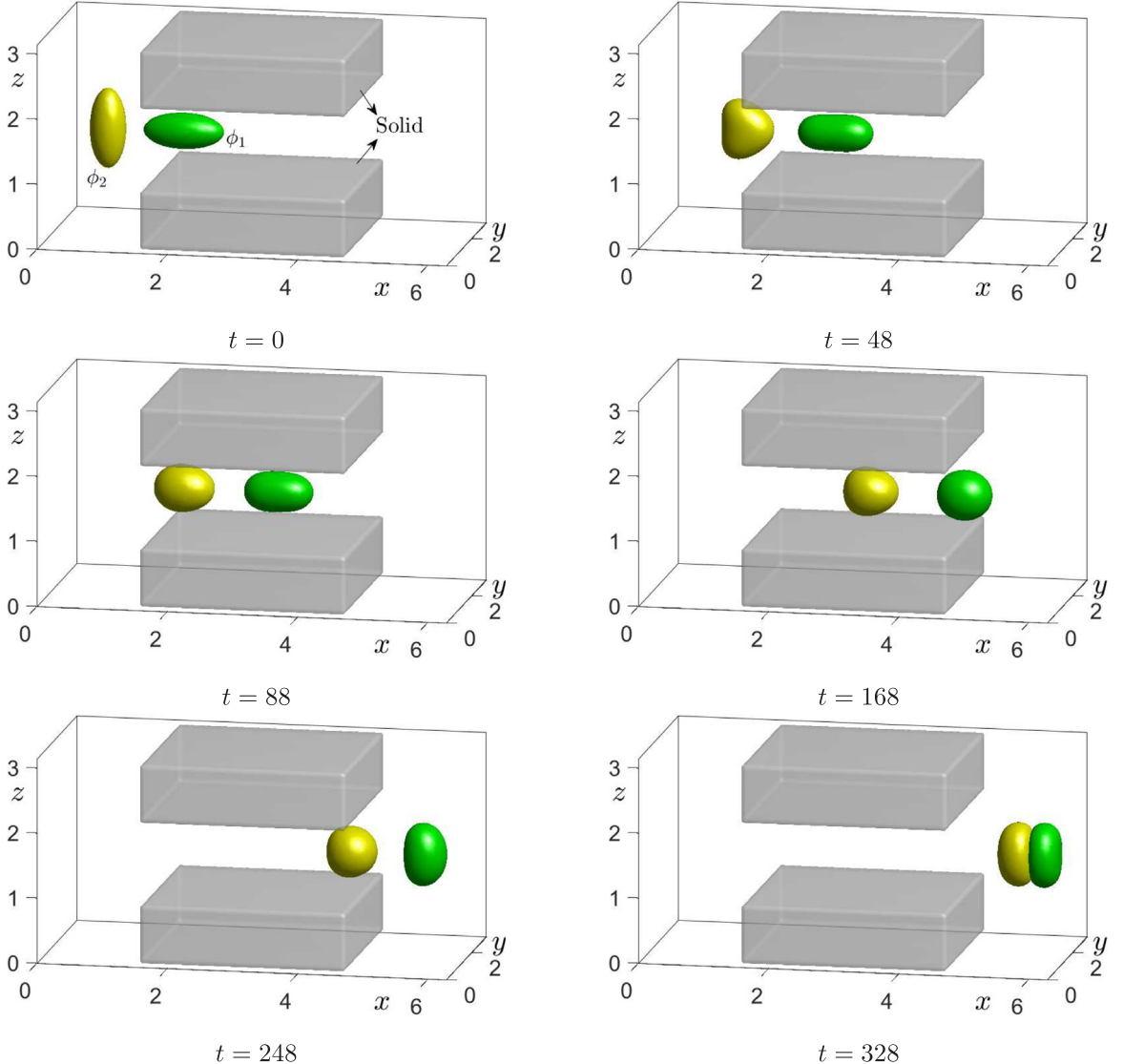
Fig. 26. Dynamic deformations of two 3D vesicles flowing through a restricted channel. Under each figure, the computational moments are illustrated.

where $\theta_1 = \tan^{-1}(y - 1.25\pi/x - 1.1\pi)$ for $x \neq 1.1\pi$ and $\theta_2 = \tan^{-1}(y - 0.75\pi/x - \pi)$ for $x \neq \pi$.

In Section 4.5, the following initial conditions are used

$$\phi_1(x, y, 0) = \tanh\left(\frac{0.25\pi - \sqrt{(x - 1.15\pi)^2/0.3 + (y - \pi)^2/1.5}}{\sqrt{2}\epsilon}\right), \tag{69}$$

$$\phi_2(x, y, 0) = \tanh\left(\frac{0.25\pi - \sqrt{(x - 0.85\pi)^2/0.3 + (y - \pi)^2/1.5}}{\sqrt{2}\epsilon}\right), \tag{70}$$

$$u(x, y, 0) = U\left(\frac{y}{\pi} - 1\right), \quad v(x, y, 0) = 0, \quad p(x, y, 0) = 0. \tag{71}$$

In Section 4.6, the initial conditions of four cases are defined as follows:

35
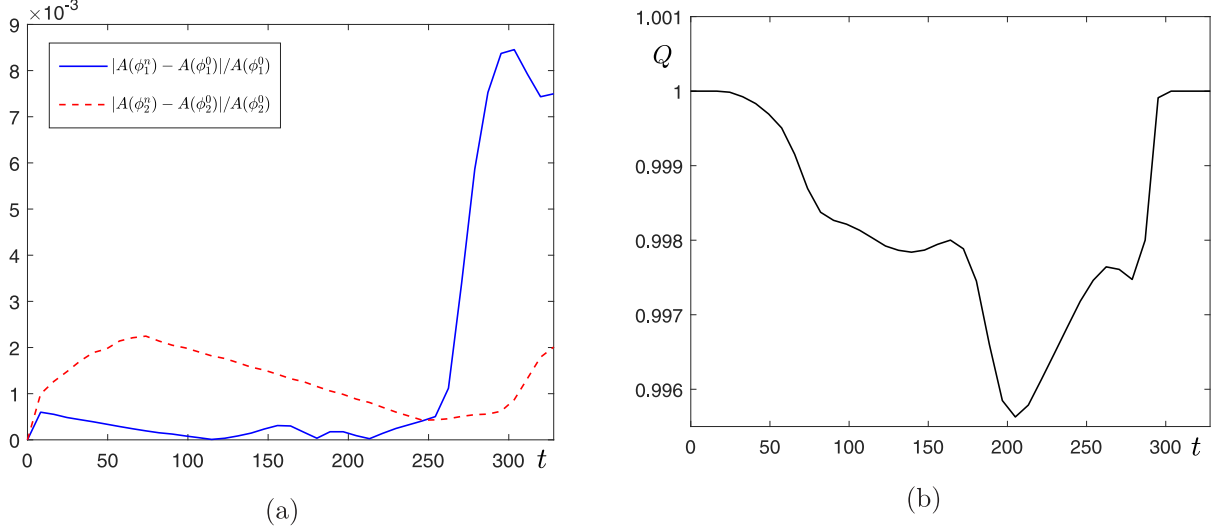
Fig. 27. Evolutions of (a) surface area ratios and (b) Q for two 3D vesicles flowing through a restricted channel.

For the first case, the following initial state of three elliptic vesicles with same size is used

$$\phi_1(x, y, 0) = \tanh\left(\frac{0.25\pi - \sqrt{(x - 1.3\pi)^2/0.3 + (y - \pi)^2/1.5}}{\sqrt{2}\epsilon}\right), \tag{72}$$

$$\phi_2(x, y, 0) = \tanh\left(\frac{0.25\pi - \sqrt{(x - \pi)^2/0.3 + (y - \pi)^2/1.5}}{\sqrt{2}\epsilon}\right), \tag{73}$$

$$\phi_3(x, y, 0) = \tanh\left(\frac{0.25\pi - \sqrt{(x - 0.7\pi)^2/0.3 + (y - \pi)^2/1.5}}{\sqrt{2}\epsilon}\right). \tag{74}$$

For the second case, we use the following initial state of three elliptic vesicles with different sizes

$$\phi_1(x, y, 0) = \tanh\left(\frac{0.3\pi - \sqrt{(x - \pi)^2/1.5 + (y - 0.76\pi)^2/0.3}}{\sqrt{2}\epsilon}\right), \tag{75}$$

$$\phi_2(x, y, 0) = \tanh\left(\frac{0.22\pi - \sqrt{(x - \pi)^2/1.5 + (y - 1.06\pi)^2/0.3}}{\sqrt{2}\epsilon}\right), \tag{76}$$

$$\phi_3(x, y, 0) = \tanh\left(\frac{0.15\pi - \sqrt{(x - \pi)^2/1.5 + (y - 1.29\pi)^2/0.3}}{\sqrt{2}\epsilon}\right). \tag{77}$$

For the third case, we use the following initial state of three adjacent circular vesicles

$$\phi_1(x, y, 0) = \tanh\left(\frac{0.18\pi - \sqrt{(x - 1.2\pi)^2 + (y - 0.79\pi)^2}}{\sqrt{2}\epsilon}\right), \tag{78}$$

$$\phi_2(x, y, 0) = \tanh\left(\frac{0.18\pi - \sqrt{(x - 0.8\pi)^2 + (y - 0.79\pi)^2}}{\sqrt{2}\epsilon}\right), \tag{79}$$

$$\phi_3(x, y, 0) = \tanh\left(\frac{0.18\pi - \sqrt{(x - \pi)^2 + (y - 1.13\pi)^2}}{\sqrt{2}\epsilon}\right). \tag{80}$$

For the last case, we define the initial conditions of three vesicles as

$$\phi_1(x, y, 0) = \tanh\left(\frac{0.25\pi - \sqrt{(x - 1.28\pi)^2/0.3 + (y - 1.2\pi)^2/1.5}}{\sqrt{2}\epsilon}\right),\tag{81}$$

$$\phi_2(x, y, 0) = \tanh\left(\frac{0.25\pi - \sqrt{(x - \pi)^2/0.3 + (y - \pi)^2/1.5}}{\sqrt{2}\epsilon}\right),\tag{82}$$

$$\phi_3(x, y, 0) = \tanh\left(\frac{0.25\pi - \sqrt{(x - 0.72\pi)^2/0.3 + (y - 0.8\pi)^2/1.5}}{\sqrt{2}\epsilon}\right).\tag{83}$$

In Section 4.7, the initial conditions of two cases in shear flow are as follows:
   The first arrangements of initial vesicles are as follows

$$\phi_1(x, y, 0) = \tanh\left(\frac{0.25\pi - \sqrt{(x - 0.72\pi)^2/0.3 + (y - 1.2\pi)^2/1.5}}{\sqrt{2}\epsilon}\right),\tag{84}$$

$$\phi_2(x, y, 0) = \tanh\left(\frac{0.25\pi - \sqrt{(x - \pi)^2/0.3 + (y - \pi)^2/1.5}}{\sqrt{2}\epsilon}\right),\tag{85}$$

$$\phi_3(x, y, 0) = \tanh\left(\frac{0.25\pi - \sqrt{(x - 1.28\pi)^2/0.3 + (y - 0.8\pi)^2/1.5}}{\sqrt{2}\epsilon}\right).\tag{86}$$

The second arrangements of initial vesicles are defined as

$$\phi_1(x, y, 0) = \tanh\left(\frac{0.25\pi - \sqrt{(x - 0.72\pi)^2/0.3 + (y - 1.2\pi)^2/1.5}}{\sqrt{2}\epsilon}\right),\tag{87}$$

$$\phi_2(x, y, 0) = \tanh\left(\frac{0.25\pi - \sqrt{(x - \pi)^2/0.3 + (y - \pi)^2/1.5}}{\sqrt{2}\epsilon}\right),\tag{88}$$

$$\phi_3(x, y, 0) = \tanh\left(\frac{0.25\pi - \sqrt{(x - 1.28\pi)^2/0.3 + (y - 1.2\pi)^2/1.5}}{\sqrt{2}\epsilon}\right).\tag{89}$$

In Section 4.8, the initial conditions of the first case are defined as

$$\phi_1(x, y, 0) = \tanh\left(\frac{0.32\pi - \sqrt{(x - 0.74\pi)^2/0.3 + (y - \pi)^2/1.5}}{\sqrt{2}\epsilon}\right),\tag{90}$$

$$\phi_2(x, y, 0) = \tanh\left(\frac{0.32\pi - \sqrt{(x - 1.12\pi)^2/0.3 + (y - \pi)^2/1.5}}{\sqrt{2}\epsilon}\right),\tag{91}$$

$$\phi_3(x, y, 0) = \tanh\left(\frac{0.32\pi - \sqrt{(x - 0.35\pi)^2/0.3 + (y - \pi)^2/1.5}}{\sqrt{2}\epsilon}\right).\tag{92}$$

The second initial conditions in Section 4.8 are defined as

$$\phi_1(x, y, 0) = \tanh\left(\frac{0.16\pi - \sqrt{(x - 0.97\pi)^2 + (y - \pi)^2}}{\sqrt{2}\epsilon}\right),\tag{93}$$

$$\phi_2(x, y, 0) = \tanh\left(\frac{0.16\pi - \sqrt{(x - 0.66\pi)^2 + (y - 1.18\pi)^2}}{\sqrt{2}\epsilon}\right),\tag{94}$$

$$\phi_3(x, y, 0) = \tanh\left(\frac{0.16\pi - \sqrt{(x - 0.66\pi)^2 + (y - 0.82\pi)^2}}{\sqrt{2}\epsilon}\right).\tag{95}$$

The last initial conditions in Section 4.8 are defined as

$$\phi_1(x, y, 0) = \tanh\left(\frac{0.42 - \sqrt{(x - 0.6\pi)^2 + (y - 0.53\pi)^2}}{\sqrt{2}\epsilon}\right),\tag{96}$$

$$\phi_2(x, y, 0) = \tanh\left(\frac{0.42 - \sqrt{(x - 1.46\pi)^2 + (y - 0.53\pi)^2}}{\sqrt{2}\epsilon}\right), \tag{97}$$

$$\phi_3(x, y, 0) = \tanh\left(\frac{0.42 - \sqrt{(x - 2.32\pi)^2 + (y - 0.53\pi)^2}}{\sqrt{2}\epsilon}\right), \tag{98}$$

$$\phi_4(x, y, 0) = \tanh\left(\frac{0.42 - \sqrt{(x - 3.18\pi)^2 + (y - 0.53\pi)^2}}{\sqrt{2}\epsilon}\right). \tag{99}$$

In Section 4.9, the initial conditions of two adjacent vesicles are defined as

$$\phi_1(x, y, z, 0) = \tanh\left(\frac{0.2\pi - \sqrt{(x - 0.61\pi)^2/0.3 + (y - \pi)^2/0.3 + (z - 0.44\pi)^2/1.5}}{\sqrt{2}\epsilon}\right), \tag{100}$$

$$\phi_2(x, y, z, 0) = \tanh\left(\frac{0.2\pi - \sqrt{(x - 0.39\pi)^2/0.3 + (y - \pi)^2/0.3 + (z - 0.56\pi)^2/1.5}}{\sqrt{2}\epsilon}\right). \tag{101}$$

In Section 4.9, the last initial conditions are defined as

$$\phi_1(x, y, z, 0) = \tanh\left(\frac{0.16\pi - \sqrt{(x - 0.62\pi)^2/1.5 + (y - 0.5\pi)^2/0.3 + (z - 0.5\pi)^2/0.3}}{\sqrt{2}\epsilon}\right), \tag{102}$$

$$\phi_2(x, y, z, 0) = \tanh\left(\frac{0.16\pi - \sqrt{(x - 0.25\pi)^2/0.3 + (y - 0.5\pi)^2/0.3 + (z - 0.5\pi)^2/1.5}}{\sqrt{2}\epsilon}\right). \tag{103}$$

References

[1] U. Seifert, Adhesion of vesicles in two dimensions, Phys. Rev. A 43 (1991) 6803–6814.

[2] H. Noguchi, G. Gompper, Fluid vesicles with viscous membranes in shear flow, Phys. Rev. Lett. 93 (2004) 258102.

[3] N.A. Nodargi, J. Kiendl, P. Bisegna, F. Caselli, L.D. Lorenzis, An isogeometric analysis formulation for red blood cell electro-deformation modeling, Comput. Methods Appl. Mech. Engrg. 338 (2018) 392–411.

[4] H. Casquero, C. Bona-Casas, D. Toshniwal, T.J.R. Hughes, H. Gomez, J. Zhang, The divergence-conforming immersed boundary method: Application to vesicle and capsule dynamics, J. Comput. Phys. 425 (2021) 109872.

[5] Q. Du, C. Liu, X. Wang, A phase field approach in the numerical study of the elastic bending energy for vesicle membranes, J. Comput. Phys. 198 (2004) 450–468.

[6] J. Lowengrub, A. Ratz, A. Voigt, Phase-field modeling of the dynamics of multicomponent vesicles: Spinodal decomposition, coarsening, budding, and fission, Phys. Rev. E 79 (2009) 031926.

[7] N. Valizadeh, T. Rabczuk, Isogeometric analysis of hydrodynamics of vesicles using a monolithic phase-field approach, Comput. Methods Appl. Mech. Engrg. 388 (2022) 114191.

[8] M. Ashour, N. Valizadeh, T. Rabczuk, Isogeometric analysis for a phase-field constrained optimization problem of morphological evolution of vesicles in eletrial fields, Comput. Methods Appl. Mech. Engrg. 377 (2022) 113669.

[9] J. Shin, D. Jeong, Y. Li, Y. Choi, J. Kim, A hybrid numerical method for the phase-field model of fluid vesicles in three-dimensional space, Internat. J. Numer. Methods Fluids 778 (2015) 63–75.

[10] G. Zou, Z. Li, X. Yang, Fully discrete discontinuous Galerkin numerical scheme with second-order temporal accuracy for the hydrodynamically coupled lipid vesicle model, J. Sci. Comput. 95 (2023) 5.

[11] M. Ashour, N. Valizadeh, T. Rabczuk, Phase-field Navier–Stokes model for vesicle doublets hydrodynamics in incompressible fluid flow, Comput. Methods Appl. Mech. Engrg. 412 (2023) 116063.

[12] J. Kim, H.G. Lee, A new conservative vector-valued Allen–Cahn eqution and its fast numerical method, Comput. Phys. Comm. 221 (2017) 102–108.

[13] S. Aihara, N. Takada, T. Takaki, Highly conservative Allen–Cahn-type multi-phase-field model and evaluation of its accuracy, Theor. Comput. Fluid Dyn. (2023) http://dx.doi.org/10.1007/s00162-023-00655-0.

[14] H. Liang, J. Xu, J. Chen, Z. Chai, B. Shi, Lattice Boltzmann modeling of wall-bounded ternary fluid flows, Appl. Math. Model. 3 (2019) 487–513.

[15] J. Yang, Phase field modeling and computation of multi-component droplet evaporation, Comput. Methods Appl. Mech. Engrg. 401 (2022) 115675.

[16] Q. Yu, Y. Li, A second-order unconditionally energy stable scheme for phase-field based multimaterial topology optimization, Comput. Methods Appl. Mech. Engrg. 405 (2023) 115876.

[17] S. Lee, Mathematical model of contractile ring-driven cytokinesis in a three-dimensional domain, Bull. Math. Biol. 80 (2) (2018) 583–597.

[18] C. Chen, X. Yang, Efficient fully discrete spectral-Galerkin scheme for the volume-conserved multi-vesicular phase-field model of lipid vesicles with adhesion potential, Commun. Math. Stat. (2022) http://dx.doi.org/10.1007/s40304-021-00278-z.

[19] C. Wang, S.M. Wise, An energy and convergent finite-difference scheme for the modified phase field crystal equation, SIAM J. Numer. Anal. 49 (2011) 945–969.

[20] K. Cheng, C. Wang, S.M. Wise, A weakly nonlinear, energy stable scheme for the strongly anisotropic Cahn–Hilliard equation and its convergence analysis, J. Comput. Phys. 405 (2020) 109109.

[21] H.G. Lee, J. Shin, J.-Y. Lee, A high-order and unconditionally energy stable scheme for the conservative Allen–Cahn equation with a nonlocal Lagrange multiplier, J. Sci. Comput. 90 (2022) 51.

[22] X. Feng, Z. Qiao, S. Sun, X. Wang, An energy-stable Smoothed Particle Hydrodynamics discretization of the Navier–Stokes–Cahn–Hilliard model for incompressible two-phase flows, J. Comput. Phys. 479 (2023) 1119977.

[23] J. Kou, X. Wang, S. Du, S. Sun, An energy stable linear numerical method for thermodynamically consistent modeling of two-phase incompressible flow in porous media, J. Comput. Phys. 451 (2022) 110854.

[24] Q. Xia, Q. Yu, Y. Li, A second-order accurate, unconditionally energy stable numerical scheme for binary fluid flows on arbitrarily curved surfaces, Comput. Methods Appl. Mech. Engrg. 384 (2021) 113987.

[25] M. Sun, X. Xiao, X. Feng, K. Wang, Modeling and numerical simulation of surfactant systems with incompressible fluid flows on surfaces, Comput. Methods Appl. Mech. Engrg. 390 (2022) 114450.

[26] Z. Liu, X. Li, A highly efficient and accurate exponential semi-implicit scalar auxiliary variable (ESI-SAV) approach for dissipative system, J. Comput. Phys. 447 (2021) 110703.

[27] Y. Gong, Q. Hong, Q. Wang, Supplementary variable method for thermodynamically consistent partial differential equations, Comput. Methods Appl. Mech. Engrg. 381 (2021) 11346.

[28] S. Wang, J. Yang, X. Pan, Highly efficient time-marching method with enhanced energy consistency for the L^2-gradient flow based two-phase incompressible fluid ssytem, Comput. Math. Appl. 139 (2023) 68–90.

[29] Q. Du, M. Li, C. Liu, Analysis of a phase field Navier–Stokes vesicle-fluid interaction model, Discrete Contin. Dyn. Syst.-B 8 (3) (2007) 539–556.

[30] S. Aland, S. Egerer, J. Lowengrub, A. Voigt, Diffuse interface models of locally inextensible vesicles in a viscous fluid, J. Comput. Phys. 227 (2014) 32–47.

[31] Z.C. Ou-Yang, J.X. Liu, Y.Z. Xie, Geometric Methods in the Elastic Theory of Membranes in Liquid Crystal Phases, No. 2, World Scientific, Singapore, 1999.

[32] P.G. Ciarlet, Mathematical Elasticity: Three-Dimensional Elasticity, Vol. 29, Springer, North-Holland, 2000.

[33] H.G. Lee, J. Kim, Regularized Dirac delta functions for phase-field models, Internat. J. Numer. Methods Engrg. 91 (2012) 269–288.

[34] H.G. Lee, J. Kim, An efficient and accurate numerical algorithm for the vector-valued Allen–Cahn equations, Comput. Phys. Comm. 183 (2012) 210–2115.

[35] H.G. Lee, J.-Y. Lee, A semi-analytical Fourier spectral method for the Allen–Cahn equation, Comput. Math. Appl. 68 (3) (2014) 174–184.

[36] E. Bretin, A. Danescu, J. Penuelas, S. Masnou, Multiphase mean curvature flows with high mobility contrasts: A phase-field approach, with applications to nanowires, J. Comput. Phys. 365 (2018) 324–349.

[37] Y. Choi, D. Jeong, S. Lee, J. Kim, Numerical implementation of the two-dimensional incompressible Navier–Stokes equation, J. KSIAM 19 (2) (2015) 103–121.

[38] J. Yang, Y. Li, J. Kim, Totally decoupled implicit-explicit linear scheme with corrected energy dissipation law for the phase-field fluid vesicle model, Comput. Methods Appl. Mech. Engrg. 399 (2022) 115330.

[39] F. Huang, J. Shen, A new class of implicit-explicit BDFk SAV schemes for general dissipative systems andd their error analysis, Comput. Methods Appl. Mech. Engrg. 392 (2022) 11418.

[40] G. Zhu, H. Chen, A. Li, S. Sun, J. Yao, Fully discrete energy stable scheme for a phase-field moving contact line model with variable densities and viscosities, Appl. Math. Model. 83 (2020) 614–639.

[41] M. Sohaib, A. Shah, Fully decoupled pressure projection scheme for the numerical solution of diffuse interface model of two-phase flow, Commun. Nonlinear Sci. Numer. Simul. 112 (2022) 106547.

[42] J. Yang, Z. Tan, J. Wang, J. Kim, Modified diffuse interface fluid model and its consistent energy-stable computation in arbitrary domains, J. Comput. Phys. 488 (2023) 112216.

[43] H. Casquero, C. Bona-Casas, H. Gomez, NURBS-based numerical proxies for red blood cells and circulating tumor cells in microscale blood flow, Comput. Methods Appl. Mech. Engrg. 316 (2017) 646–667.

[44] I.V. Tasso, G.C. Buscaglia, A finite element method for vescous membranes, Comput. Methods Appl. Mech. Engrg. 255 (2013) 226–237.

[45] Z. Qiao, Z. Zhang, T. Tang, An adaptive time-stepping strategy for the molecular beam epitaxy models, SIAM J. Sci. Comput. 33 (3) (2011) 1395–1414.

[46] S. Hu, Z. Lin, D. Wang, X.-P. Wang, An unconditionally stable threshold dynamics method for the Willmore flow, Jpn. J. Ind. Appl. Math. (2023) http://dx.doi.org/10.1007/s13160-023---590-x.

[47] A. Laadhari, P. Saramito, C. Misbah, Vesicle tumbling inhibited by inertia, Phys. Fluids 24 (2012) 031901.

[48] V. Kantsler, V. Steinberg, Transition to tumbling and two regimes of tumblingmotion of a vesicle in shear flow, Phys. Rev. Lett. 96 (2006) 036001.

[49] S.Y. Park, P. Dimitrakopoulos, Transient dynamics of an elastic capsule in a microfluidic constriction, Soft Matter 9 (2013) 8844–8855.

[50] T. Ye, N. Phan-Thien, B.C. Kooh, C.T. Lim, A file of red blood cells in tube flow: A three-dimensional numerical study, J. Appl. Phys. 116 (2014) 562–568.

[51] T. Ye, H.X. Shi, N. Phan-Thien, C.T. Lim, Y. Li, Numerical design of a miscrofluidic chip for probing mechanical properties of cells, J. Biomech. 84 (2019) 103–112.

[52] M. Bergmann, J. Hovnanian, A. Iollo, An accurate cartesian method for incompressible flows with moving boundaries, Commun. Comput. Phys. 15 (2014) 1266–1290.

[53] J.-W. Choi, H.G. Lee, D. Jeong, J. Kim, An unconditionally gradient stable numerical method for solving the Allen–Cahn equation, Physica A 388 (2009) 1791–1803.

[54] L.L. Xiao, S. Chen, C.S. Lin, Y. Liu, Simulation of single red blood cell flowing through a microvessel stenosis using dissipative particle dynamics, Mol. Cell Boimech. 11 (1) (2014) 67–85.